Theory of high-efficiency adiabatic frequency conversion in coupled microrings

Luis Cortes-Herrera [*], Xiaotong He, Jaime Cardenas, and Govind P. Agrawal
Institute of Optics, University of Rochester, Rochester, New York 14627, USA

Adiabatic frequency conversion (AFC) in microring resonators is a promising alternative for integrated, tunable frequency shifting of optical signals. However, the efficiency of AFC in a single-ring resonator is limited to below 80% for symmetric input pulses with a single peak. This is the consequence of a poor match between the pulse shape and the ring's impulse response. To overcome this limitation, we propose inducing AFC over two coupled rings rather than a single ring. We analyze the process's efficiency using temporal coupled mode theory (TCMT). We show that two-ring AFC can attain an efficiency of 97% in the limit of negligible intrinsic ring loss. To explain this higher AFC efficiency, we analyze two-ring AFC as a linear operator of rank two in the vector space of finite-energy pulses. We represent the AFC operator as a 2×2 matrix and examine its singular value decomposition. In this way we analyze the dependence of the two-ring AFC efficiency on the input pulse shape and the TCMT parameters.

I. INTRODUCTION

In photonics, frequency conversion is usually realized via nonlinear wave mixing. The advent of integrated photonics in recent years has enabled broadband wave mixing on a chip with a compact footprint [1–4]. Despite its successes, nonlinear wave mixing has several inherent limitations [5–7]. First, it demands a high-power optical pump, which impedes on-chip integration. Second, nonlinear wave mixing must obey the conservation of photon energy. Consequently, to tune the output signal's frequency, one must change the frequency of either the input signal or the pump. Third, efficient wave mixing requires phase matching. This requirement restricts both the waveguide geometry and the range of possible output frequencies.

Adiabatic frequency conversion (AFC) is a promising alternative for frequency shifting. AFC is the phenomenon in which light excites an optical cavity's mode, the cavity's refractive index is temporally modulated, and the light follows the cavity's instantaneous resonance frequency [8,9]. This process is called adiabatic because it was shown numerically [9] that it preserves the adiabatic invariant of a harmonic oscillator [10,11]. In contrast to nonlinear wave mixing, AFC does not require optical pumping or phase matching and is not restricted by photon-energy conservation. Moreover, its output frequency can be tuned by adjusting the magnitude of index modulation within the cavity. As a result, AFC can be used to realize tunable frequency conversion in a photonic chip. AFC has been demonstrated through injection of charge carriers in silicon cavities [12–16] and in semiconductor-based metasurfaces [17], through the optical Kerr effect in a silica toroidal cavity [18], and through the Pockels effect in bulk [19] and integrated [20] lithium-niobate resonators.

So far, most theoretical work on AFC has focused either on its modeling and description [8,9,21–23] or on its proposal for novel applications [8,24–26]. Discussion of the efficiency of AFC has attracted less attention. It was found in Ref. [27] that AFC of a Gaussian pulse in an all-pass resonator (e.g., a microring coupled to a bus waveguide) can yield an energy efficiency of 74%. In Ref. [28] we investigated the fundamental limits of AFC efficiency in an all-pass resonator employing temporal coupled-mode theory (TCMT) [29–33]. There we demonstrated that the process's efficiency is limited by a Schwarz inequality. Consequently, near-unity efficiency can be attained only when two conditions are satisfied. First, the intrinsic loss of the resonator must be small compared to the input pulse's bandwidth and the bus-resonator coupling rate. Second, in accordance with the matched-filter principle [34,35], the incident pulse must resemble the ring's time-reversed impulse response, in this case, a truncated increasing exponential. Hence, for a symmetric single-lobe pulse (such as a Gaussian pulse), the maximum AFC efficiency is limited to less than 80% [27,28]. It is desirable to increase the efficiency of AFC for such optical pulses because they are employed in optical communications [5,36].

In this paper we use TCMT to demonstrate that the AFC of symmetric single-lobe pulses can achieve a considerably higher efficiency of 97% when it is induced over two coupled microrings, rather than over a single ring. To explain the increased efficiency in this coupled-ring system, we examine AFC as a linear operator of rank two in the Hilbert space of finite-energy pulses (i.e., square-integrable functions). We show that this operator can be understood as the composition of two linear maps: the first one representing the pre-modulation loading of the input into the rings' modal amplitudes, and the second one representing their postmodulation unloading into the frequency-shifted output. Then we project the AFC operator's image and coimage onto orthonormal bases to represent the loading map, the unloading map,
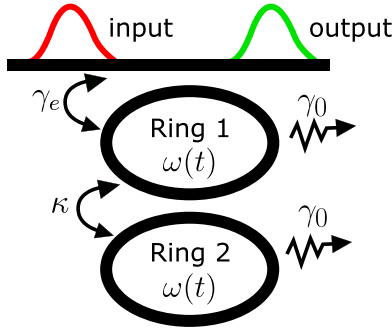
---

[*] lcortesh@ur.rochester.edu

FIG. 1. Schematic diagram of the photonic circuit for two-ring adiabatic frequency conversion.

and the AFC operator as 2×2 matrices. We study these matrices' singular value decomposition and show how these decompositions govern the AFC process's efficiency. We evaluate our analytical results numerically in terms of the rings' TCMT parameters. We note that TCMT has been used to describe accurately the response of time-varying resonators [23,24,26]. Thus, its use in this paper is appropriate.

The rest of the paper is organized as follows. In Sec. II we introduce the two-ring photonic circuit we propose for high-efficiency AFC, and we describe its operation. We present the TCMT equations governing it and write their analytical solution in the limit of strong and fast temporal modulations. In Sec. III we examine the solution of Sec. II as an operator in the vector space of finite-energy pulses, given by the composition of the loading and an unloading maps. We characterize the image and coimage of each of these maps. In Sec. IV we project the AFC's linear operator into distinct orthonormal bases for its image and coimage to obtain a 2×2 matrix representation for it. Then we propose a singular value decomposition (SVD) of this matrix representation and discuss its use to examine the AFC efficiency. In Sec. V we study the dependence of the rings' impulse response on the device parameters. This study aids the interpretation of the numerical results in subsequent sections. In Sec. VI we investigate numerically the SVD of the ring loading and ring unloading maps, which combine to form the complete two-ring AFC process. In Sec. VII we analyze the SVD of the full AFC process using the results of the prior sections. In Sec. VIII we examine the AFC of a symmetric, single-lobe pulse in our proposed two-ring network and compare our results with AFC in a single-ring resonator. We interpret our results based on the SVD analysis of the preceding sections. In Sec. IX we review the paper's conclusions.

II. DESCRIPTION OF THE PHOTONIC CIRCUIT AND THE AFC LINEAR OPERATOR

Figure 1 shows the proposed photonic circuit for high-efficiency AFC. It consists of two identical evanescently coupled ring resonators (Ring 1 and Ring 2), one of them (Ring 1) coupled to a bus waveguide. An optical pulse with carrier frequency equal to the rings' original resonance frequency ω_0 is injected through the bus. Afterwards the rings' resonance frequency is modulated to induce AFC on the stored light. The frequency-shifted output exits through the

bus waveguide. We note that the circuit in Fig. 1 is identical to one proposed in Ref. [37]. However, the ring modulation in Ref. [37] is sinusoidal, and the one in this work is monotonic. Hence, the mechanisms for frequency conversion are fundamentally different [9], and so is their corresponding analysis and optimization.

Let $a_j(t)$ $(j = 1, 2)$ denote the amplitude of the field in the ring resonators at time t. As conventional in TCMT [29–33], these are normalized so that $|a_j(t)|^2$ equals the energy in Ring j at time t. Similarly, let $s_{\text{in}}(t)$ and $s_{\text{out}}(t)$ denote the amplitude of the pulse coming into and out of Ring 1. These are normalized so that $|s_{\text{in}}(t)|^2$ is the instantaneous incoming power at time t, and $|s_{\text{out}}(t)|^2$, the instantaneous outgoing power at time t. Of course, as pointed out in Ref. [32], this normalization of $s_{\text{in}}(t)$ and $s_{\text{out}}(t)$ is accurate only when $s_{\text{in}}(t)$ and $s_{\text{out}}(t)$ are sufficiently narrowband for the variation of the waveguide's modal profile to be negligible.

Employing TCMT [29–33], we find that the temporal evolution of the column vector $a(t) = (a_1(t), a_2(t))^T$ is governed by the ordinary differential equation

$$\frac{\mathrm{d}a}{\mathrm{d}t} = H(t)a(t) + k s_{\text{in}}(t). \tag{1}$$

Here k a constant column vector, and $H(t)$ a time-dependent square matrix, both given by

$$k = (\sqrt{2\gamma_e}, 0)^T, \tag{2}$$

$$H(t) = \begin{pmatrix} -i\omega(t) - \gamma_1 & i\kappa \\ i\kappa^* & -i\omega(t) - \gamma_2 \end{pmatrix}. \tag{3}$$

In Eq. (2), γ_e is the coupling rate between Ring 1 and the bus waveguide. In Eq. (3), $\omega(t)$ is the rings' instantaneous frequency; κ, the complex-valued coupling rate from Ring 2 to Ring 1; γ_1, the decay rate of Ring 1; and γ_2, the decay rate of Ring 2.

In accordance to Fig. 1, we assume that only Ring 1 is coupled to the bus. Hence, we write the decay rates γ_1 and γ_2 as

$$\gamma_1 = \gamma_e + \gamma_0, \quad \gamma_2 = \gamma_0. \tag{4}$$

where γ_0 is the intrinsic decay rate of each ring, assumed to be the same for the two identical rings.

From TCMT, we also obtain an expression for the output $s_{\text{out}}(t)$ in terms of the input $s_{\text{in}}(t)$ and the rings' amplitude $a(t)$. This is given by

$$s_{\text{out}}(t) = \exp(i\phi)[s_{\text{in}}(t) - k^\dagger a(t)], \tag{5}$$

where ϕ is a constant phase that depends on the locations where $s_{\text{in}}(t)$ and $s_{\text{out}}(t)$ are defined [31]. The negative sign before $k^\dagger a(t)$ is necessary to ensure the output energy equals the input energy when the ring frequencies are constant and there is zero intrinsic ring loss (i.e., when $\gamma_0 = 0$). This can be verified by writing the TCMT equations in the frequency domain and invoking Parseval's theorem. This negative sign is also consistent with perturbative treatment of TCMT in Ref. [31]. We take $\exp(i\phi) = -1$ for convenience and without loss of generality.

To examine AFC, we consider the case in which $\omega(t)$ changes monotonically. For simplicity, and in the interest of studying fast, efficient AFC, we assume the modulation

of $\omega(t)$ takes place rapidly compared to any other relevant timescale except the carrier optical frequency. Thus, as in Ref. [28], we write $\omega(t)$ as

$$\omega(t) = \omega_0 + \Delta\Theta(t - t_m). \tag{6}$$

Here ω_0 is the value of $\omega(t)$ premodulation; $(\omega_0 + \Delta)$, its value postmodulation; t_m, the time at which modulation is applied; and $\Theta(t)$, the Heaviside unit-step function. Substituting Eq. (6) into Eq. (3), the coefficient matrix $H(t)$ may then be written in the analogous form

$$H(t) = H_0 + (H_m - H_0)\Theta(t - t_m). \tag{7}$$

Naturally, H_0 is the value of $H(t)$ before modulation, with $\omega(t)$ in Eq. (3) replaced by ω_0, and H_m, the value of $H(t)$ after modulation, with $\omega(t)$ replaced by $(\omega_0 + \Delta)$.

Using Eq. (7) for $H(t)$, it is straightforward to integrate Eq. (1). For investigating the AFC efficiency, we need only consider $a(t)$ for $t \geqslant t_m$. For $t < t_m$, $a(t)$ oscillates at the original frequency ω_0, which we assume is filtered out after AFC. The solution of Eq. (1) for $t \geqslant t_m$ is given by

$$a(t) = \exp\left[H_m(t - t_m)\right]a(t_m)$$
$$+ \int_{t_m}^{t} dt' \exp[H_m(t - t')]k s_{\text{in}}(t'), \quad \text{for } t \geqslant t_m, \tag{8}$$

where $a(t_m)$, the rings' amplitude at the time of modulation t_m, is given by

$$a(t_m) = \int_{-\infty}^{t_m} dt \exp\left[H_0(t_m - t)\right]k s_{\text{in}}(t). \tag{9}$$

Henceforth, we assume that the ring modulation is such that the frequency-shift magnitude $|\Delta|$ is large compared to the bandwidth of the input $s_{\text{in}}(t)$. In this case we may accurately neglect the second term in the right-hand side of Eq. (8), as in Ref. [28]. This neglect is akin to the rotating-wave approximation in the theory of optical resonance in two-level atoms [38].

Because of this assumed large modulation, we may also neglect the first term in Eq. (5), by supposing that any output $s_{\text{out}}(t)$ oscillating at the original frequency is filtered out. Therefore, under this approximation, we may substitute Eq. (8) into Eq. (5) to obtain

$$s_{\text{out}}(t) = k^\dagger \Theta(t - t_m) \exp\left[H_m(t - t_m)\right]a(t_m). \tag{10}$$

Together, Eqs. (9) and (10) provide a linear operator transforming the input $s_{\text{in}}(t)$ into the frequency-shifted output $s_{\text{out}}(t)$. Equation (9) describes the loading of $s_{\text{in}}(t)$ into the ring amplitude $a(t_m)$ at time t_m, and Eq. (10) describes the unloading of the ring amplitudes $a(t_m)$ into the output pulse $s_{\text{out}}(t)$ in the bus waveguide.

To close this section, we discuss sufficient conditions on the refractive-index modulation for coupled-ring AFC to be accurately described by Eqs. (1) and (6) and thus achieve high net efficiency. These conditions are for modulation to be both homogeneous in space (over the coupled rings) and fast in time (compared to the other TCMT timescales). If the modulation is spatially inhomogeneous and occurs with a speed comparable to or faster than the rings' free spectral range, it may induce energy leakage into the rings' neighboring longitudinal modes [9,23,39]. Usually, only the output

spectrum within a free spectral range is useful, so the spectral broadening due to the excitation of a ring's other longitudinal modes results in a reduction of the AFC efficiency. However, if the modulation is either spatially homogeneous or slow compared to the rings' free spectral range, dynamic mode coupling is inhibited [9,23,39], and we need only consider a single mode per ring (and per polarization) in Eq. (1). Nonetheless, for efficient AFC, index modulation must be fast compared to the other TCMT timescales, so long as the ring modulation is spatially homogeneous enough to avoid dynamical mode coupling. This is because, as modulation is induced, the rings' energy continuously decays in time due to coupling to the bus waveguide and due to intrinsic loss. Thus, a slower index modulation results in a decrease in AFC efficiency, and we may restrict attention to the fast ring modulation described in Eq. (6).

III. INNER-PRODUCT ANALYSIS OF THE AFC LINEAR OPERATOR AND ITS EFFICIENCIES

For the following analysis, we identify the input and output pulses, $s_{\text{in}}(t)$ and $s_{\text{out}}(t)$, as vectors in the vector space of finite-energy pulses, or mathematically, the Hilbert space of square-integrable functions of time, L^2. Thus, we employ Dirac notation and identify them with the kets $|s_{\text{in}}(t)\rangle$ and $|s_{\text{out}}(t)\rangle$, respectively. This vector space has a natural inner product, $\langle f(t)|g(t)\rangle$, defined as

$$\langle f(t)|g(t)\rangle \equiv \int_{-\infty}^{\infty} dt\, f^*(t)g(t). \tag{11}$$

In this notation, the energy E_{in} of the input pulse and the energy E_{out} of the output pulse are given by

$$E_{\text{in}} = \langle s_{\text{in}}(t)|s_{\text{in}}(t)\rangle, \tag{12}$$

$$E_{\text{out}} = \langle s_{\text{out}}(t)|s_{\text{out}}(t)\rangle. \tag{13}$$

Of course, E_{out} depends on the energy E_r of the rings at the time of modulation t_m. Correspondingly, E_r given by

$$E_r = a^\dagger(t_m)a(t_m). \tag{14}$$

In this Dirac notation, we may rewrite Eqs. (9) and (10), which govern AFC. These become the abstract equations

$$a(t_m) = \hat{T}_{\text{in}}|s_{\text{in}}(t)\rangle, \tag{15}$$

$$|s_{\text{out}}(t)\rangle = \hat{T}_{\text{out}}a(t_m). \tag{16}$$

Here $\hat{T}_{\text{in}}$ and $\hat{T}_{\text{out}}$ are linear maps. Specifically, $\hat{T}_{\text{in}}$ is a linear map from L^2 to the vector space of two-dimensional, complex-valued vectors, $\mathbb{C}^2$; and $\hat{T}_{\text{out}}$ is a linear map from $\mathbb{C}^2$ to L^2.

For subsequent analysis, we wish to write explicit expressions for $\hat{T}_{\text{in}}$ and $\hat{T}_{\text{out}}$ in this Dirac notation. To do so, it is convenient to introduce some auxiliary functions. Let $[A]_{mn}$ be the m, n element of the matrix A. Then we define the functions $u_{nm}(t, 0)$ and $u_{nm}(t, \Delta)$ as

$$u_{nm}(t, 0) = [\exp(H_0 t)]_{nm},$$
$$u_{nm}(t, \Delta) = [\exp(H_m t)]_{nm}. \tag{17}$$

Here Δ stands for the postmodulation frequency shift, as in Eq. (6). Physically, $u_{nm}(t, 0)$ and $u_{nm}(t, \Delta)$ represent the impulse-response functions of the two rings before and after the index modulation. In Appendix A we provide explicit expressions for them and examine their properties that are relevant to our study. In terms of these impulse response functions, we can write $\hat{T}_{\text{in}}$ and $\hat{T}_{\text{out}}$ as

$$\hat{T}_{\text{in}} = \sqrt{2\gamma_e} \begin{pmatrix} \langle u_{11}^*(t_m - t, 0)| \\ \langle u_{21}^*(t_m - t, 0)| \end{pmatrix}, \tag{18}$$

$$\hat{T}_{\text{out}} = \sqrt{2\gamma_e}(|u_{11}(t - t_m, \Delta)\rangle, \quad |u_{12}(t - t_m, \Delta)\rangle), \tag{19}$$

where the conjugation of the bra vectors results from the definition of the inner product in Eq. (11).

An immediate collorary of Eqs. (15) and (16) is that they constitute a linear map of $|s_{\text{in}}(t)\rangle$ to $|s_{\text{out}}(t)\rangle$ through their composition. Let us denote this map by $\hat{T}$. Then we have

$$|s_{\text{out}}(t)\rangle = \hat{T}|s_{\text{in}}(t)\rangle. \tag{20}$$

It follows that $\hat{T}$ is a linear map from L^2 to L^2, i.e., a linear operator in L^2. Comparing Eq. (20) to Eqs. (15) and (16), we find that

$$\hat{T} = \hat{T}_{\text{out}}\hat{T}_{\text{in}}. \tag{21}$$

Substituting Eq. (18) for $\hat{T}_{\text{in}}$ and Eq. (19) for $\hat{T}_{\text{out}}$ into (21), we get the explicit expression for $\hat{T}$,

$$\hat{T} = 2\gamma_e \sum_{j=1}^{2} |u_{1j}(t - t_m, \Delta)\rangle\langle u_{j1}^*(t_m - t, 0)|. \tag{22}$$

The preceding reformulation of AFC in Dirac notation allows us to write succinct expressions for the AFC process's efficiencies. In turn, we show below that these succinct expressions lend themselves to further analysis. We define the AFC's efficiency η as the ratio of the energy E_{out} in the frequency-shifted output to the energy of the input E_{in}. Substituting Eqs. (12) and (13), it follows that η is given by

$$\eta = \frac{\langle s_{\text{out}}(t)|s_{\text{out}}(t)\rangle}{\langle s_{\text{in}}(t)|s_{\text{in}}(t)\rangle},$$
$$= \frac{\langle s_{\text{in}}(t)|\hat{T}^\dagger\hat{T}|s_{\text{in}}(t)\rangle}{\langle s_{\text{in}}(t)|s_{\text{in}}(t)\rangle}, \tag{23}$$

where we used Eq. (20) for $|s_{\text{out}}(t)\rangle$.

As discussed above, the AFC process can be understood as a succession of two constituent processes: the loading $\hat{T}_{\text{in}}$ of the input pulse until the modulation time t_m and the unloading $\hat{T}_{\text{out}}$ of the output pulse after t_m. Hence, it is useful and physically significant to define efficiencies for each of these processes. Let η_{in} be the efficiency of the loading process, with map $\hat{T}_{\text{in}}$; and η_{out}, the efficiency of the unloading process, with map $\hat{T}_{\text{out}}$. From Eqs. (12), (14), and (18), it follows that

$$\eta_{\text{in}} = \frac{a^\dagger(t_m)a(t_m)}{\langle s_{\text{in}}(t)|s_{\text{in}}(t)\rangle},$$
$$= \frac{\langle s_{\text{in}}(t)|\hat{T}_{\text{in}}^\dagger\hat{T}_{\text{in}}|s_{\text{in}}(t)\rangle}{\langle s_{\text{in}}(t)|s_{\text{in}}(t)\rangle}; \tag{24}$$

and from Eqs. (13), (14), and (19), it follows that

$$\eta_{\text{out}} = \frac{\langle s_{\text{out}}(t)|s_{\text{out}}(t)\rangle}{a^\dagger(t_m)a^(t_m)},$$
$$= \frac{a^\dagger(t_m)\hat{T}_{\text{out}}^\dagger\hat{T}_{\text{out}}a(t_m)}{a^\dagger(t_m)a(t_m)}. \tag{25}$$

Intuitively, the efficiency of the complete AFC process is the product of the efficiency of each process. Thus, provided $E_r > 0$, we have

$$\eta = \eta_{\text{in}}\eta_{\text{out}}. \tag{26}$$

As a consequence of its expression in Eq. (18), $\hat{T}_{\text{in}}$ is nonzero over vector components in the subspace of L^2 spanned by $|u_{11}^*(t_m - t, 0)\rangle$ and $|u_{21}^*(t_m - t, 0)\rangle$. Let us denote this subspace as $\mathcal{V}_{\text{in}}$, and let $\hat{P}_{\text{in}}$ be the projection operator into $\mathcal{V}_{\text{in}}$. Because $\hat{T}_{\text{in}}$ is nonzero only $\mathcal{V}_{\text{in}}$, we may write

$$\hat{T}_{\text{in}} = \hat{T}_{\text{in}}\hat{P}_{\text{in}}. \tag{27}$$

Then, substituting Eq. (27) into Eq. (24), and supposing that $\hat{P}|s_{\text{in}}(t)\rangle \neq 0$, we may factor the loading efficiency η_{in} as

$$\eta_{\text{in}} = \eta_{\text{in}}^{(p)}\eta_p. \tag{28}$$

In Eq. (28), η_p is the projection efficiency, defined as the ratio

$$\eta_p = \frac{\langle s_{\text{in}}(t)|\hat{P}_{\text{in}}^\dagger\hat{P}_{\text{in}}|s_{\text{in}}(t)\rangle}{\langle s_{\text{in}}(t)|s_{\text{in}}(t)\rangle},$$
$$= \frac{\langle s_{\text{in}}^{(p)}(t)|s_{\text{in}}^{(p)}(t)\rangle}{\langle s_{\text{in}}^{(p)}(t)|s_{\text{in}}^{(p)}(t)\rangle + \langle s_{\text{in}}^{(o)}(t)|s_{\text{in}}^{(o)}(t)\rangle}. \tag{29}$$

Here $|s_{\text{in}}^{(p)}(t)\rangle$ and $|s_{\text{in}}^{(o)}(t)\rangle$ are the components of $|s_{\text{in}}(t)\rangle$ parallel and orthogonal to $\mathcal{V}_{\text{in}}$. In terms of the projector $\hat{P}_{\text{in}}$, these can be expressed as

$$\left|s_{\text{in}}^{(p)}(t)\right\rangle = \hat{P}_{\text{in}}|s_{\text{in}}(t)\rangle,$$
$$\left|s_{\text{in}}^{(o)}(t)\right\rangle = (1 - \hat{P}_{\text{in}})|s_{\text{in}}(t)\rangle. \tag{30}$$

In Eq. (28), $\eta_{\text{in}}^{(p)}$ is the projected loading efficiency, defined as the ratio

$$\eta_{\text{in}}^{(p)} = \frac{\left\langle s_{\text{in}}^{(p)}(t)\right|\hat{T}_{\text{in}}^\dagger\hat{T}_{\text{in}}\left|s_{\text{in}}^{(p)}(t)\right\rangle}{\left\langle s_{\text{in}}^{(p)}(t)|s_{\text{in}}^{(p)}(t)\right\rangle}. \tag{31}$$

Given Eqs. (27) and (28), it is useful to interpret the loading $\hat{T}_{\text{in}}$ as a composition of two other maps. From Eq. (27), the fist map is the projection $\hat{P}_{\text{in}}$ of the input $|s_{\text{in}}(t)\rangle$ into the two-dimensional vector space $\mathcal{V}_{\text{in}} \in L^2$. From Eq. (29), the energy lost in this process is that in the component $|s_{\text{in}}^{(o)}(t)\rangle$, orthogonal to $\mathcal{V}_{\text{in}}$. The second map is the action of $\hat{T}_{\text{in}}$ on the projected input $|s_{\text{in}}^{(p)}(t)\rangle \in \mathcal{V}_{\text{in}}$. The efficiency of this process is $\eta_{\text{in}}^{(p)}$, given by Eq. (31).

Given the second line in Eq. (29), the projection efficiency η_p can be interpreted as a function of the ratio of $\langle s_{\text{in}}^{(o)}(t)|s_{\text{in}}^{(o)}(t)\rangle$ to $\langle s_{\text{in}}^{(p)}(t)|s_{\text{in}}^{(p)}(t)\rangle$. The quantity $\langle s_{\text{in}}^{(o)}(t)|s_{\text{in}}^{(o)}(t)\rangle$ is non-negative, so η_p is maximized with respect to it when $\langle s_{\text{in}}^{(o)}(t)|s_{\text{in}}^{(o)}(t)\rangle$ vanishes, and η_p equals unity.

Furthermore, η_{in} depends on $\langle s_{\text{in}}^{(o)}(t)|s_{\text{in}}^{(o)}(t)\rangle$ only through the factor of η_p in Eq. (28). This has two consequences on the maximization of η_{in}. First, η_{in} is also maximized with respect to $\langle s_{\text{in}}^{(o)}(t)|s_{\text{in}}^{(o)}(t)\rangle$ when it equals zero. Second, the maximum loading efficiency η_{in} over any input nonzero $|s_{\text{in}}(t)\rangle \in L^2$ equals the maximum of the projected loading efficiency $\eta_{\text{in}}^{(p)}$ over any nonzero projected input $|s_{\text{in}}^{(p)}(t)\rangle \in \mathcal{V}_{\text{in}}$. Written mathematically,

$$\max_{|s_{\text{in}}(t)\rangle \neq 0} \eta_{\text{in}} = \max_{|s_{\text{in}}^{(p)}(t)\rangle \neq 0} \eta_{\text{in}}^{(p)}. \tag{32}$$

This result is significant because the right-hand side of Eq. (32) can be maximized via techniques of finite-dimensional linear algebra, as we discuss below in Sec. IV.

Having analyzed the implications of Eq. (27) in the properties of the loading efficiency η_{in}, we next do the same for the overall AFC efficiency η. Substituting Eq. (27) into Eq. (21), it follows directly that

$$\hat{T} = \hat{T}\hat{P}_{\text{in}}. \tag{33}$$

Then, just as for η_{in} in Eq. (28) and again assuming $|s_{\text{in}}^{(p)}(t)\rangle \neq 0$, the overall efficiency η can be factored as

$$\eta = \eta^{(p)}\eta_p, \tag{34}$$

where $\eta^{(p)}$ is the projected AFC efficiency and is given by the ratio

$$\eta^{(p)} = \frac{\langle s_{\text{in}}^{(p)}(t)|\hat{T}^{\dagger}\hat{T}|s_{\text{in}}^{(p)}(t)\rangle}{\langle s_{\text{in}}^{(p)}(t)|s_{\text{in}}^{(p)}(t)\rangle}, \tag{35}$$

and η_p is again the projection efficiency in Eq. (29).

Naturally, substituting Eq. (28) into Eq. (26) and comparing with Eq. (34) yields

$$\eta^{(p)} = \eta_{\text{in}}^{(p)}\eta_{\text{out}}, \tag{36}$$

which has the intuitive meaning that the overall projected efficiency $\eta^{(p)}$ is that of the projected loading followed by ring unloading.

Again, we note that the net efficiency η depends on the energy $\langle s_{\text{in}}^{(o)}(t)|s_{\text{in}}^{(o)}(t)\rangle$ only through η_p, as indicated in Eq. (34). Thus, just as η_{in}, η is maximized with respect to the nonnegative $\langle s_{\text{in}}^{(o)}(t)|s_{\text{in}}^{(o)}(t)\rangle$ when the latter vanishes. In addition, we have

$$\max_{|s_{\text{in}}(t)\rangle \neq 0} \eta = \max_{|s_{\text{in}}^{(p)}(t)\rangle \neq 0} \eta^{(p)}, \tag{37}$$

just as η_{in} in Eq. (32). Once more, Eq. (37) is significant because the maximization of its right-hand side can be performed via methods of finite-dimensional linear algebra, which we do in Sec. IV.

We conclude this section with a few remarks on the interpretation of the AFC efficiency η. Within the phenomenological framework of TCMT, we defined η in Eq. (23) as the ratio of the output energy at the target output frequency, to

the input energy. It follows from Eq. (23) that η is independent of the frequency shift Δ, so long as it is sufficiently large compared to the other TCMT time rates that filtering of the output results in negligible loss. Moreover, we show in Sec. VII that η has a tight upper bound of unity. These properties of the AFC energy efficiency η seemingly contradict the intuition that the input light consists of a stream of photons, with energy proportional to their frequency; so the output AFC energy should depend on the frequency shift and have no upper limit, at least in the limit of negligible intrinsic ring loss.

Nonetheless, this photon-stream intuition is indeed compatible with our analysis's results because TCMT is known to be accurate only for narrowband optical excitations [32]. Thus, if the induced frequency shift is small compared to the input pulse's carrier frequency, TCMT is accurate, and one may safely neglect the change in the photon energy due to the frequency shift. This is usually the case in AFC of telecom and optical signals, where the ratio of the frequency shift to the carrier frequency is on the order of 10^{-5} to 10^{-3} [12,18–20].

Furthermore, we show in the Supplemental Material [40], via a quantum-optical analysis of the AFC process, that the photon-stream intuition is correct: in the absence of intrinsic loss, AFC in a set of coupled resonators preserves the system's photon-number statistics but not its energy statistics. Additionally, we show that, to the accuracy of the input-output formalism, popular in quantum optics [41–44], the energy efficiency η of Eq. (23), obtained via TCMT, can be interpreted as a mean photon-number efficiency when the rings-waveguide system is initially in a coherent waveguide state. With this interpretation, the fact that η is independent of the the frequency shift and bounded by unity is intuitive. Additionally, with this interpretation as a photon-number efficiency, Eq. (23) for η can be extended beyond the accuracy of TCMT. Nonetheless, the input-output formalism itself is still applicable only to optical excitations with a bandwith smaller than that of the ring-waveguide coupling, as explained in the Supplemental Material [40].

IV. AFC MATRIX REPRESENTATION AND SINGULAR VALUE DECOMPOSITION

We aim to fully dissect the AFC efficiency η, determine its upper bounds and examine its dependence on the rings' TCMT parameter and the input pulse shape. To do so, we next introduce orthonormal bases for the image and coimage of the AFC operator $\hat{T}$. In this way we can represent and analyze it as a matrix.

The coimage of $\hat{T}$ is the orthogonal complement to its nullspace. Hence, it is the subspace of L^2 spanned by $\{|u_{11}^*(t_m - t, 0)\rangle, |u_{21}^*(t_m - t, 0)\rangle\}$, denoted by $\mathcal{V}_{\text{in}}$ in Sec. III. From Eq. (22), the image of $\hat{T}$ is the subspace of L^2 spanned by $\{|u_{11}(t - t_m, \Delta)\rangle, |u_{12}(t - t_m, \Delta)\rangle\}$. We denote this subspace by $\mathcal{V}_{\text{out}}$.

As shown in Appendix A, $|u_{11}^*(t_m - t, 0)\rangle$ and $|u_{21}^*(t_m - t, 0)\rangle$ are not mutually orthogonal unless $\gamma_0 = 0$. Therefore, in general they do not form an orthonormal basis of $\mathcal{V}_{\text{in}}$. Nonetheless, we generate an orthonormal basis $\{|n_1^{(\text{in})}\rangle, |n_2^{(\text{in})}\rangle\}$ from them through Gram-Schmidt

orthonormalization [45,46]. We define these unit vectors of $\mathcal{V}_{\text{in}}$ so they satisfy

$$
\begin{aligned}
\langle n_l^{(\text{in})} | n_m^{(\text{in})} \rangle &= \delta_{lm}, \\
|n_2^{(\text{in})} \rangle &\propto |u_{21}^*(t_m - t, 0)\rangle, \\
|n_1^{(\text{in})} \rangle &\in \mathcal{V}_{\text{in}}, \\
\langle n_1^{(\text{in})} | u_{11}^*(t_m - t, 0) \rangle &> 0, \\
\langle n_2^{(\text{in})} | u_{21}^*(t_m - t, 0) \rangle &> 0.
\end{aligned}
\tag{38}
$$

Here δ_{lm} is the Kronecker delta. Explicit expressions for $|n_1^{(\text{in})}\rangle$ and $|n_2^{(\text{in})}\rangle$ which satisfy Eq. (38) are given in Appendix B. In Eq. (38) we choose $|n_2^{(\text{in})}\rangle$ to be proportional to $|u_{21}^*(t_m - t, 0)\rangle$, rather than have $|n_1^{(\text{in})}\rangle$ proportional to $|u_{11}^*(t_m - t, 0)\rangle$. We find that this choice in Eq. (38) simplifies the interpretation of the results in Sec. VIII.

Analogously, we apply Gram-Schmidt orthonormalization to $|u_{11}(t - t_m, \Delta)\rangle$ and $|u_{12}(t - t_m, \Delta)\rangle$ to obtain an orthonormal basis $\{|n_1^{(\text{out})}\rangle, |n_2^{(\text{out})}\rangle\}$ for the image $\mathcal{V}_{\text{out}}$. This output basis satisfies relations analogous to those in Eq. (38), with $|u_{11}^*(t_m - t, 0)\rangle$ replaced by $|u_{11}(t - t_m, \Delta)\rangle$, $|u_{21}^*(t_m - t, 0)\rangle$ by $|u_{12}(t - t_m, \Delta)\rangle$, and $\mathcal{V}_{\text{in}}$ by $\mathcal{V}_{\text{out}}$. This is shown in Appendix B, where explicit expressions for $|n_1^{(\text{out})}\rangle$ and $|n_2^{(\text{out})}\rangle$ are provided as well.

With these orthonormal bases for $\mathcal{V}_{\text{in}}$ and $\mathcal{V}_{\text{out}}$, we next follow orthonormal representation theory [45] (popular in quantum mechanics [47,48]) to represent the projected input vector $|s_{\text{in}}^{(p)}(t)\rangle$, and the output vector $|s_{\text{out}}(t)\rangle$ with column vectors, x_{in} and x_{out}; and the linear maps $\hat{T}_{\text{in}}$, $\hat{T}_{\text{out}}$, and $\hat{T}$, with square matrices M_{in}, M_{out}, and M, respectively. In this way, we obtain

$$
\begin{aligned}
|s_{\text{in}}^{(p)}(t)\rangle &= \left(|n_1^{(\text{in})}\rangle, \quad |n_2^{(\text{in})}\rangle \right) x_{\text{in}}, \\
|s_{\text{out}}(t)\rangle &= \left(|n_1^{(\text{out})}\rangle, \quad |n_2^{(\text{out})}\rangle \right) x_{\text{out}}, \\
\hat{T}_{\text{in}} &= M_{\text{in}} \begin{pmatrix} \langle n_1^{(\text{in})}| \\ \langle n_2^{(\text{in})}| \end{pmatrix}, \\
\hat{T}_{\text{out}} &= \left(|n_1^{(\text{out})}\rangle, \quad |n_2^{(\text{out})}\rangle \right) M_{\text{out}}, \\
\hat{T} &= \left(|n_1^{(\text{out})}\rangle, \quad |n_2^{(\text{out})}\rangle \right) M \begin{pmatrix} \langle n_1^{(\text{in})}| \\ \langle n_2^{(\text{in})}| \end{pmatrix}.
\end{aligned}
\tag{39}
$$

Here $x_{\text{in}}, x_{\text{out}} \in \mathbb{C}^2$, and $M_{\text{in}}, M_{\text{out}}, M \in \mathbb{C}^{2\times 2}$, i.e., they are complex-valued two-dimensional vectors and 2×2 matrices, respectively. Again, matrix multiplication in Eq. (39) is implied. Expressions for the matrices M_{in}, M_{out}, and M are given by

$$
\begin{aligned}
M_{\text{in}} &= \sqrt{2\gamma_e} \begin{pmatrix} \langle u_{11}^*(t_m - t, 0)|n_1^{(\text{in})}\rangle & \langle u_{11}^*(t_m - t, 0)|n_2^{(\text{in})}\rangle \\ \langle u_{21}^*(t_m - t, 0)|n_1^{(\text{in})}\rangle & \langle u_{21}^*(t_m - t, 0)|n_2^{(\text{in})}\rangle \end{pmatrix}, \\
M_{\text{out}} &= \sqrt{2\gamma_e} \begin{pmatrix} \langle n_1^{(\text{out})}|u_{11}(t - t_m, \Delta)\rangle & \langle n_1^{(\text{out})}|u_{12}(t - t_m, \Delta)\rangle \\ \langle n_2^{(\text{out})}|u_{11}(t - t_m, \Delta)\rangle & \langle n_2^{(\text{out})}|u_{12}(t - t_m, \Delta)\rangle \end{pmatrix}, \\
M &= M_{\text{out}} M_{\text{in}}.
\end{aligned}
\tag{40}
$$

More explicit expressions for M_{in} and M_{out}, amenable for numerical evaluation, are presented in Appendix B.

Next, we express the efficiencies $\eta_{\text{in}}^{(p)}$, η_{out}, and $\eta^{(p)}$ in the representation of Eq. (39). To do so, we substitute Eq. (39) into their corresponding expressions [Eqs. (31), (25), and (35), respectively] and leverage the orthonormality of the input and output bases. In this way, we write

$$
\begin{aligned}
\eta_{\text{in}}^{(p)} &= \frac{x_{\text{in}}^\dagger M_{\text{in}}^\dagger M_{\text{in}} x_{\text{in}}}{x_{\text{in}}^\dagger x_{\text{in}}}, \\
\eta_{\text{out}} &= \frac{a^\dagger(t_m) M_{\text{out}}^\dagger M_{\text{out}} a(t_m)}{a^\dagger(t_m) a(t_m)}, \\
\eta^{(p)} &= \frac{x_{\text{in}}^\dagger M^\dagger M x_{\text{in}}}{x_{\text{in}}^\dagger x_{\text{in}}}.
\end{aligned}
\tag{41}
$$

The expression $(x^\dagger A x)/(x^\dagger x)$ for a square matrix A and a column vector x is called their Rayleigh quotient in the context of linear algebra [49].

The advantage of introducing the representation Eq. (39) and writing the efficiencies $\eta_{\text{in}}^{(p)}$, η_{out}, and $\eta^{(p)}$ as Rayleigh quotients is that these are well understood in finite-dimensional linear algebra [49,50]. Thus, we can investigate them with the robust analytical and numerical techniques of this area. In particular, to study Eq. (41) we find it useful to introduce the singular value decomposition (SVD) of the matrices M_{in}, M_{out}, and M. Let $A \in C^{n\times n}$. Then the SVD of A is a matrix decomposition of the form [50,51]

$$
A = \sum_{j=1}^{n} \sigma_j w_j v_j^\dagger.
\tag{42}
$$

Here $\sigma_j \geqslant 0$ are called the singular values of A; w_j and v_j are two orthonormal sets of vectors, called the left singular vectors and right singular vectors of A. Every matrix A, even nonsquare ones, has a SVD. Moreover, the singular values σ_j are uniquely determined, and for square A, the vectors w_j and v_j are uniquely determined up to arbitrary phase factors, so long as the σ_j are distinct [51]. Also, a matrix's SVD is a step in many algorithms in numerical linear algebra, so its computation is a well-studied problem.

Substituting the SVD of the matrices M_{in}, M_{out}, and M into Eq. (41), we may write the efficiencies $\eta_{\text{in}}^{(p)}$, η_{out}, and

$\eta^{(p)}$ as

$$\eta_{\text{in}}^{(p)} = \sum_{j=1}^{2} p_j(M_{\text{in}}, x_{\text{in}}) \sigma_j^2(M_{\text{in}}),$$

$$\eta_{\text{out}} = \sum_{j=1}^{2} p_j(M_{\text{out}}, a(t_m)) \sigma_j^2(M_{\text{out}}),$$

$$\eta^{(p)} = \sum_{j=1}^{2} p_j(M, x_{\text{in}}) \sigma_j^2(M). \tag{43}$$

As the notation suggests, $\sigma_j(A)$ is the jth singular value of the matrix A. The factors $p_j(A, x)$ are relative weights satisfying $p_j(A, x) \geqslant 0$ and $\sum_{j=1}^{2} p_j(A, x) = 1$ and are given by

$$p_j(A, x) = \frac{x^\dagger v_j(A) v_j^\dagger(A) x}{x^\dagger x}. \tag{44}$$

In accordance to Eq. (42), $v_j(A)$ is the jth right singular vector of A.

Equation (43) is one of the main results of this paper. It implies that the efficiencies $\eta_{\text{in}}^{(p)}$, η_{out}, and $\eta^{(p)}$ are weighted sums of the square of the singular values of their corresponding matrix. Moreover, according to Eq. (44), the weight for each σ_j^2 is given by the normalized squared projection of the input column vector [either x_{in} or $a(t_m)$] into the jth right singular vector, v_j.

A corollary of Eq. (43) is that the extrema for the efficiencies $\eta_{\text{in}}^{(p)}$, η_{out}, and $\eta^{(p)}$ over their corresponding input are given by

$$\max_{|s_{\text{in}}^{(p)}(t)\rangle \neq 0} \eta_{\text{in}}^{(p)} = \sigma_{\max}^2(M_{\text{in}}),$$

$$\max_{a(t_m) \neq 0} \eta_{\text{out}} = \sigma_{\max}^2(M_{\text{out}}),$$

$$\max_{|s_{\text{in}}^{(p)}(t)\rangle \neq 0} \eta^{(p)} = \sigma_{\max}^2(M) \tag{45}$$

and

$$\min_{|s_{\text{in}}^{(p)}(t)\rangle \neq 0} \eta_{\text{in}}^{(p)} = \sigma_{\min}^2(M_{\text{in}}),$$

$$\min_{a(t_m) \neq 0} \eta_{\text{out}} = \sigma_{\min}^2(M_{\text{out}}),$$

$$\min_{|s_{\text{in}}^{(p)}(t)\rangle \neq 0} \eta^{(p)} = \sigma_{\min}^2(M). \tag{46}$$

Here $\sigma_{\max}(A)$ ($\sigma_{\min}(A)$) is the maximum (minimum) singular value of A.

Moreover, Eqs. (43) and (44) provide prescriptions for how to attain the extrema in Eqs. (45) and (46). The maxima (minima) for $\eta_{\text{in}}^{(p)}$ and $\eta^{(p)}$ occur when $|s_{\text{in}}^{(p)}(t)\rangle$ has components in the input basis $\{|n_1^{(\text{in})}\rangle, |n_2^{(\text{in})}\rangle\}$ proportional to the right singular vector v_j corresponding to $\sigma_{\max}(M_{\text{in}})$ and $\sigma_{\max}(M)$ [$\sigma_{\min}(M_{\text{in}})$ and $\sigma_{\min}(M)$], respectively. Similarly, the maximum (minimum) of η_{out} occurs when the amplitude vector $a(t_m)$ is proportional to the right singular vector v_j corresponding to $\sigma_{\max}(M_{\text{out}})$ [$\sigma_{\min}(M_{\text{out}})$].

Lastly, the SVD of M_{in}, M_{out}, and M also prescribes how the energy in the extrema of Eqs. (45) and (46) is distributed over the images of $\hat{T}_{\text{in}}$, $\hat{T}_{\text{out}}$, and $\hat{T}$, respectively. When the

maximum (minimum) of $\eta_{\text{in}}^{(p)}$ occurs, the amplitude vector $a(t_m)$ at the time of modulation is proportional to the left singular vector w_j corresponding to $\sigma_{\max}(M_{\text{in}})$ ($\sigma_{\min}(M_{\text{in}})$). Similarly, when the maxima (minima) of η_{out} and $\eta^{(p)}$ occur, the frequency-shifted output $|s_{\text{out}}(t)\rangle$ has components in the output basis $\{|n_1^{(\text{out})}\rangle, |n_2^{(\text{out})}\rangle\}$ proportional to the left singular vector w_j corresponding to $\sigma_{\max}(M_{\text{out}})$ and $\sigma_{\max}(M)$ [$\sigma_{\min}(M_{\text{out}})$ and $\sigma_{\min}(M)$], respectively.

It is important to note that Eq. (45) gives us not only the maxima for the projected efficiencies $\eta_{\text{in}}^{(p)}$ and $\eta^{(p)}$, but also the maxima for the overall efficiencies η_{in} and η. Substituting Eq. (45) into Eqs. (32) and (37), we obtain

$$\max_{|s_{\text{in}}(t)\rangle \neq 0} \eta_{\text{in}} = \sigma_{\max}^2(M_{\text{in}}),$$

$$\max_{|s_{\text{in}}(t)\rangle \neq 0} \eta = \sigma_{\max}^2(M). \tag{47}$$

Just as discussed after Eq. (45), the maxima in Eq. (47) are attained when $|s_{\text{in}}(t)\rangle = |s_{\text{in}}^{(p)}(t)\rangle$ and $|s_{\text{in}}^{(p)}(t)\rangle$ has components x_{in} [as in Eq. (39)] proportional to the right singular vector v_j corresponding to $\sigma_{\max}(M_{\text{in}})$ or $\sigma_{\max}(M)$. Again, then the output is proportional to the corresponding left singular vector w_j. Unlike $\eta_{\text{in}}^{(p)}$ and $\eta^{(p)}$, however, the minima of η_{in} and η are zero and not the minimum singular values in Eq. (46). These vanishing efficiencies appear when $|s_{\text{in}}^{(p)}(t)\rangle = 0$, i.e., when $|s_{\text{in}}(t)\rangle = |s_{\text{in}}^{(o)}(t)\rangle$. This is a consequence of Eqs. (27) and (33).

V. NUMERICAL ANALYSIS OF THE TWO-RING IMPULSE-RESPONSE FUNCTIONS

In the following sections, we evaluate numerically the analytical results of Secs. III to IV to quantitatively characterize two-ring AFC and its efficiency. In this section we start by examining the impulse-response functions $u_{nm}(t, \Delta)$, which govern the AFC process as discussed in Sec. III.

Let $\bar{u}_{nm}(t) = u_{nm}(t, \Delta) \exp[i(\omega_0 + \Delta)t]$ be the envelopes of the impulse response functions $u_{nm}(t, \Delta)$. We plot the envelope functions $\bar{u}_{11}(t)$ and $\bar{u}_{21}(t)$ in Fig. 2 for $\gamma_0 = 0$ and for different values of $|\kappa|/\gamma_e$. Increasing values of γ_0 merely cause the envelopes $\bar{u}_{nm}(t)$ to decay more rapidly with t. As seen in Appendix A, $\bar{u}_{12}(t) = \bar{u}_{21}(t)(\kappa/\kappa^*)$, so plotting $\bar{u}_{12}(t)$ in addition to $\bar{u}_{21}(t)$ is redundant.

It is important to observe the general shape of the envelopes $\bar{u}_{nm}(t)$. This is for two reasons. First, as discussed in Sec. III, $u_{11}^*(t_m - t, 0)$ and $u_{21}^*(t_m - t, 0)$ span the vector space $\mathcal{V}_{\text{in}} \in L^2$ over which the input efficiency η_{in} and the overall AFC efficiency η are nonzero. Second, as discussed in Secs. III and IV, $u_{11}(t - t_m, \Delta)$ and $u_{12}(t - t_m, \Delta)$ span the image $\mathcal{V}_{\text{out}} \in L^2$ of $\hat{T}_{\text{out}}$ (and hence $\hat{T}$).

We first note the behavior of $\bar{u}_{11}(t)$ and $\bar{u}_{21}(t)$ at $t = 0$. In Fig. 2 we observe that we always have $\bar{u}_{11}(0) = 1$ and $\bar{u}_{21}(0) = 0$. Consequently, at $t = 0$, $\bar{u}_{11}(t)$ is discontinuous from the left, but $\bar{u}_{21}(t)$ is continuous. Furthermore, we show in Appendix A that we always have $\frac{du_{11}(0)}{dt} = -\gamma_1$ and $\frac{du_{21}(0)}{dt} = i\kappa^*$.

In contrast, the qualitative behavior of $\bar{u}_{11}(t)$ and $\bar{u}_{21}(t)$ for $t > 0$ depends on the ratio between the interring coupling and the waveguide-ring coupling, i.e., $|\kappa|/\gamma_e$. We
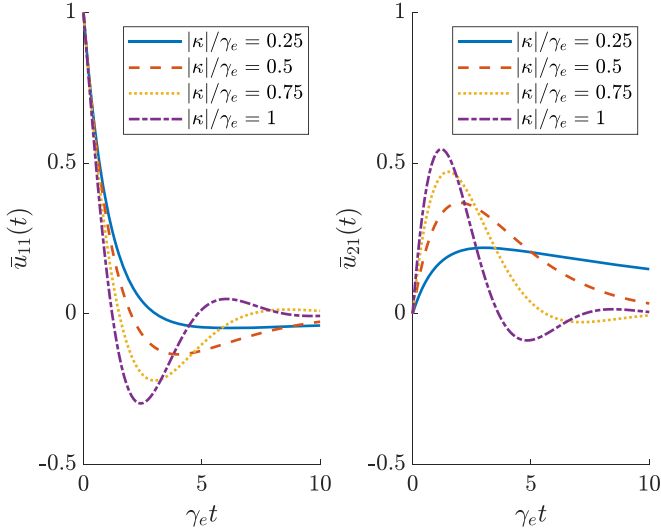
FIG. 2. Plots of the envelopes $\bar{u}_{nm}(t)$ of the impulse-response functions $u_{nm}(t, \Delta)$ for $\gamma_0 = 0$ and for different values of $|\gamma|/\gamma_e$. For ease of visualization, we take $\text{Re}\{\kappa\} = 0$ and $\text{Im}\{\kappa\} \geqslant 0$.
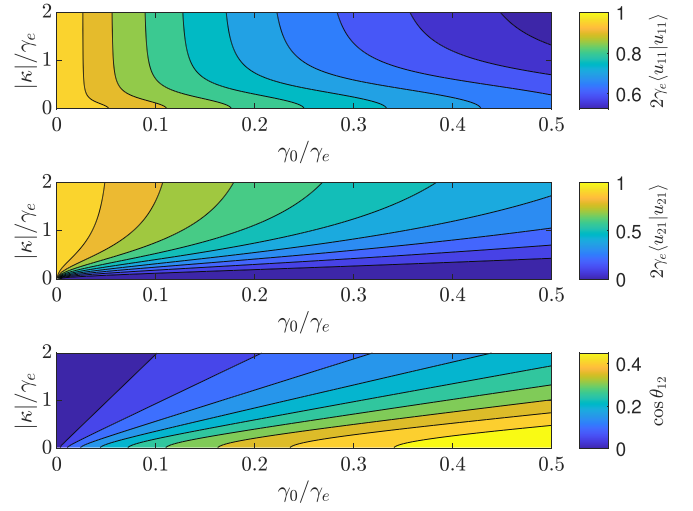

FIG. 3. Contour plots of the normalized squared norms $2\gamma_e \langle u_{11}|u_{11}\rangle$ and $2\gamma_e \langle u_{21}|u_{21}\rangle$, and of the effective cosine $\cos\theta_{12}$ as functions of the normalized coupling magnitude $|\kappa|/\gamma_e$ and the normalized intrinsic loss γ_0/γ_e.

show in Appendix A that, depending on the value of this ratio, interring coupling can be underdamped, critically damped, or overdamped, just as the motion of a damped harmonic oscillator [52,53].

If $|\kappa|/\gamma_e > 1/2$, then interring coupling is underdamped. In this case $\bar{u}_{11}(t)$ and $\bar{u}_{21}(t)$ oscillate around zero with a frequency of $\sqrt{|\kappa|^2 - (\gamma_e/2)^2}$, but their oscillation amplitude decays exponentially at the ring-averaged decay rate of $\bar{\gamma} = (\gamma_1 + \gamma_2)/2$.

If $|\kappa|/\gamma_e = 1/2$, then interring coupling is critically damped. In this case, $\bar{u}_{11}(t)$ and $\bar{u}_{21}(t)$ become the products of two factors. The first factor is still an exponentially decreasing envelope, decaying with the rate $\bar{\gamma}$. The second factor is an affine function of time. Hence, $\bar{u}_{11}(t)$ and $\bar{u}_{21}(t)$ still decay with the rate $\bar{\gamma}$ for $t \gg \gamma_e^{-1}$.

If $|\kappa|/\gamma_e < 1/2$, then interring coupling is overdamped. In this case $\bar{u}_{11}(t)$ and $\bar{u}_{21}(t)$ become the sum of two exponentially decaying terms: one decaying with a rate of $\bar{\gamma} + \sqrt{(\gamma_e/2)^2 - |\kappa|^2}$, and the other with a rate of $\bar{\gamma} - \sqrt{(\gamma_e/2)^2 - |\kappa|^2}$. Naturally, the latter term dominates for large t because it decays more slowly. In Appendix A we show that, for overdamped interring coupling, both envelopes $\bar{u}_{11}(t)$ and $\bar{u}_{21}(t)$ attain exactly one extremum. Moreover, $\bar{u}_{11}(t)$ always becomes negative for sufficiently large t, but $\bar{u}_{21}(t)$ has the same phase for any t.

Next, we examine the inner products of the impulse-response functions $u_{nm}(t, \Delta)$ with each other and with themselves, i.e., their squared norms. These quantities are relevant to our analysis of AFC because they determine the matrices M_{in} and M_{out} (as seen in Sec. IV and Appendix B) and thus govern the projected efficiencies $\eta_{\text{in}}^{(p)}$, η_{out}, and $\eta^{(p)}$ through Eq. (43). Specifically, we analyze three dimensionless quantities. Two of these are the normalized squared norms $2\gamma_e \langle u_{11}|u_{11}\rangle = 2\gamma_e \langle u_{11}(t, \Delta)|u_{11}(t, \Delta)\rangle$ and $2\gamma_e \langle u_{21}|u_{21}\rangle = 2\gamma_e \langle u_{21}(t, \Delta)|u_{21}(t, \Delta)\rangle$. The third of these is the effective cosine $\cos\theta_{12}$ between $|u_{11}\rangle$ and $|u_{21}\rangle$,

defined as

$$\cos\theta_{12} \equiv \frac{|\langle u_{11}|u_{21}\rangle|}{\sqrt{\langle u_{11}|u_{11}\rangle \langle u_{21}|u_{21}\rangle}}. \tag{48}$$

Clearly $\cos\theta_{12} \geqslant 0$, and $\cos\theta_{12} = 0$ if and only if $|u_{11}\rangle$ and $|u_{21}\rangle$ are orthogonal. Furthermore, as a consequence of the Schwarz inequality, $\cos\theta_{12} \leqslant 1$ and $\cos\theta_{12} = 1$ if and only if $|u_{11}\rangle \propto |u_{21}\rangle$. Therefore, $\cos\theta_{12}$ can be interpreted as a measure of the collinearity of $|u_{11}\rangle$ and $|u_{21}\rangle$. Below we show that these three quantities govern the SVD of M_{in} and M_{out}.

To study the quantities $2\gamma_e \langle u_{11}|u_{11}\rangle$, $2\gamma_e \langle u_{21}|u_{21}\rangle$, and $\cos\theta_{12}$, we note that they depend only on the rings' TCMT parameters: the waveguide-ring coupling γ_e, the intrinsic decay rate γ_0, and the interring coupling κ. Additionally, we find in Appendix A that they depend only on the magnitude of κ, rather than on both its magnitude and phase. So we need only investigate $2\gamma_e \langle u_{11}|u_{11}\rangle$, $2\gamma_e \langle u_{21}|u_{21}\rangle$, and $\cos\theta_{12}$ as functions of the two dimensionless ratios $|\kappa|/\gamma_e$ and γ_0/γ_e to understand their general behavior for nonzero γ_e.

Figure 3 shows contour plots of $2\gamma_e \langle u_{11}|u_{11}\rangle$, $2\gamma_e \langle u_{21}|u_{21}\rangle$, and $\cos\theta_{12}$ as functions of $|\kappa|/\gamma_e$ and γ_0/γ_e. We examine first their values for the ideal case of $\gamma_0 = 0$. As seen readily in Fig. 3 and shown analytically in Appendix A, for $\gamma_0 = 0$, $2\gamma_e \langle u_{11}|u_{11}\rangle = 2\gamma_e \langle u_{11}|u_{11}\rangle = 1$, and $\cos\theta_{12} = 0$, independently of the value of $|\kappa|/\gamma_e$. Then, as γ_0/γ_e increases from zero, both $2\gamma_e \langle u_{11}|u_{11}\rangle$ and $2\gamma_e \langle u_{21}|u_{21}\rangle$ decrease monotonically, while $\cos\theta_{12}$ increases monotonically. From the formulas for $\langle u_{11}|u_{11}\rangle$, $\langle u_{21}|u_{21}\rangle$, and $\langle u_{11}|u_{21}\rangle$ in Appendix A, it follows that $\langle u_{11}|u_{11}\rangle$ and $\langle u_{21}|u_{21}\rangle$ converge to 0, and that $\cos\theta_{12}$ converges to $1/\sqrt{2}$ in such a way that

$$\cos\theta_{12} < 1/\sqrt{2}, \tag{49}$$

for nonzero γ_e and $|\kappa|$. In other words, $\cos\theta_{12}$ converges to $1/\sqrt{2}$ from below as γ_0/γ_e tends to infinity and $|\kappa|/\gamma_e$ remains finite.

Although both $2\gamma_e \langle u_{11}|u_{11}\rangle$ and $2\gamma_e \langle u_{21}|u_{21}\rangle$ decrease with increasing γ_0/γ_e, we always have

$$\langle u_{11}|u_{11}\rangle \geqslant \langle u_{21}|u_{21}\rangle, \tag{50}$$

and equality is achieved if and only if $\gamma_0 = 0$, as shown in Appendix A, though their difference decreases with increasing $|\kappa|$.

Additionally, the rates at which the squared norms decrease and the effective cosine increases with γ_0/γ_e evidently depends on $|\kappa|/\gamma_e$. Increasing $|\kappa|/\gamma_e$ causes $2\gamma_e \langle u_{11}|u_{11}\rangle$ to decrease more rapidly with γ_0/γ_e, but it causes $2\gamma_e \langle u_{21}|u_{21}\rangle$ to decrease more slowly with γ_0/γ_e. On the other hand, $\cos\theta_{12}$ increases with γ_0/γ_e more rapidly with smaller $|\kappa|/\gamma_e$.

The dependence of the squared norms on $|\kappa|/\gamma_e$ makes intuitive sense. This is because, as depicted in Fig. 1, Ring 1 is directly coupled to the bus waveguide, but Ring 2 is not. Therefore, if $|\kappa| \ll \gamma_0$, energy coupled from Ring 1 into Ring 2 is quickly dissipated, causing $2\gamma_e \langle u_{21}|u_{21}\rangle$ to be small. But if $|\kappa|$ increases beyond γ_0, energy can accumulate in $u_{21}(t, \Delta)$, and energy in $u_{11}(t, \Delta)$ leaks into Ring 2. This also explains why we always have $\langle u_{11}|u_{11}\rangle \geqslant \langle u_{21}|u_{21}\rangle$ for $\gamma_0 > 0$, and why their difference decreases with $|\kappa|$.

To understand the increase of $\cos\theta_{12}$ with γ_0/γ_e, we note that increasing γ_0 enhances damping in the impulse responses $u_{11}(t, \Delta)$ and $u_{21}(t, \Delta)$ common to both rings. This pushes the behavior of both impulse-response functions towards exponential decay, thus increasing their collinearity, as measured by $\cos\theta_{12}$. However, this increase in their rate of exponential decay cannot make $u_{11}(t, \Delta)$ and $u_{21}(t, \Delta)$ fully collinear (i.e., linearly dependent), due to their difference in initial conditions, as pointed out in the discussion of Fig. 2. As a result, $\cos\theta_{12}$ converges to $1/\sqrt{2}$ for large γ_0 rather than unity. As seen in Fig. 3, the increase in collinearity between $u_{11}(t, \Delta)$ and $u_{21}(t, \Delta)$ is inhibited by an increase in $|\kappa|$ as well. This is because larger $|\kappa|$ either inhibits exponential decay (if interring coupling is overdamped) or keeps the amplitude oscillations of $u_{11}(t, \Delta)$ and $u_{21}(t, \Delta)$ out of phase (if interring coupling is underdamped).

To conclude this section, we add a remark on the critical damping condition, $|\kappa| = \gamma_e/2$. It is that this condition corresponds to a so-called exceptional point of the rings' parameter space [54,55], where the matrix $H(t)$ of Eq. (1) becomes nondiagonalizable. At this exceptional point, the eigenvalues of $H(t)$ are no longer holomorphic functions of the TCMT parameters and acquire a branch-cut topology [54,55]. This singular behavior has recently been leveraged to design novel high-sensitivity photonic densors and adiabatic mode converters, among other devices [55–57]. Nonetheless, at the exceptional point $|\kappa| = \gamma_e/2$, the exponential matrices $\exp(H_0 t)$ and $\exp(H_m t)$ in Eq. (17) remain well defined and continuous [58] with respect to the TCMT parameters. Furthermore, these matrices are expressible as Neumann series [46] in terms of perturbations to the TCMT parameters, as in quantum-mechanical time-dependent perturbation theory [47]. Thus, these matrices are holomorphic in the TCMT parameters, and so are their elements, the impulse responses $u_{nm}(t, 0)$ and $u_{nm}(t, \Delta)$. Hence, the AFC dynamics and efficiency exhibit no extraordinary behavior at the exceptional point $|\kappa| = \gamma_e/2$.

VI. NUMERICAL SVD OF THE LOADING AND UNLOADING MAPS

With the results of the previous section, we now study numerically the SVD of AFC in the two-ring system of Fig. 1. First, for this section we study the SVD of the individual loading and unloading matrices, M_{in} and M_{out}. We then use these results to investigate the SVD of the full AFC process, with matrix representation $M = M_{\text{out}} M_{\text{in}}$ in Sec. VII.

In Appendix C we perform a partial analytical SVD of both M_{in} and M_{out}. There we obtain the left singular vectors of M_{in}, the right singular vectors of M_{out}, and the singular values of both matrices. First, we examine the singular values, but we also examine the singular vectors later in this section. As we demonstrate in Appendix C, M_{in} and M_{out} have identical singular values, i.e., we have

$$\sigma_j(M_{\text{in}}) = \sigma_j(M_{\text{out}}), \tag{51}$$

assuming these are ordered either in ascending or descending order. Thus we need only consider those of M_{in}, $\sigma_j(M_{\text{in}})$. In Appendix C we show that these may be written in terms of the inner products of the impulse-response functions $u_{nm}(t, \Delta)$ as

$$\frac{\sigma_{\max}^2(M_{\text{in}})}{2\gamma_e} = \frac{\langle u_{11}|u_{11}\rangle + \langle u_{21}|u_{21}\rangle}{2}$$
$$+ \sqrt{\left(\frac{\langle u_{11}|u_{11}\rangle - \langle u_{21}|u_{21}\rangle}{2}\right)^2 + |\langle u_{11}|u_{11}\rangle u_{21}|^2},$$

$$\frac{\sigma_{\min}^2(M_{\text{in}})}{2\gamma_e} = \frac{\langle u_{11}|u_{11}\rangle + \langle u_{21}|u_{21}\rangle}{2}$$
$$- \sqrt{\left(\frac{\langle u_{11}|u_{11}\rangle - \langle u_{21}|u_{21}\rangle}{2}\right)^2 + |\langle u_{11}|u_{11}\rangle u_{21}|^2}. \tag{52}$$

We note how these singular values depend on the inner product $\langle u_{11}|u_{21}\rangle$. If $\langle u_{11}|u_{21}\rangle = 0$, then, as a consequence of Eq. (50), $\sigma_{\max}(M_{\text{in}}) = 2\gamma_e \langle u_{11}|u_{11}\rangle$, and $\sigma_{\min}(M_{\text{in}}) = 2\gamma_e \langle u_{21}|u_{21}\rangle$. Nonetheless, $\langle u_{11}|u_{21}\rangle = 0$ happens if and only if $\gamma_0 = 0$, as seen in Fig. 3. Nonzero $\langle u_{11}|u_{21}\rangle$ then increases $\sigma_{\max}^2(M_{\text{in}})$ above $2\gamma_e \langle u_{11}|u_{11}\rangle$, and decreases $\sigma_{\min}^2(M_{\text{in}})$ below $2\gamma_e \langle u_{21}|u_{21}\rangle$. Therefore, nonorthogonality of $u_{11}(t, \Delta)$ $u_{21}(t, \Delta)$ further splits the singular values $\sigma_j(M_{\text{in}})$. In particular, the splitting of the squares of the singular values is analogous to the eigenvalue splitting of a quantum-mechanical two-level system when interaction between its original eigenstates is introduced. This mathematical similarity arises because the squared singular values σ_j^2 of M_{in} and M_{out} are the eigenvalues of the Hermitian matrices $M_{\text{in}}^\dagger M_{\text{in}}$ and $M_{\text{out}}^\dagger M_{\text{out}}$, as is well known in linear algebra [50,51] and as we leverage in Appendix C.

Naturally, the Schwarz inequality limits the maximum singular-value splitting due to nonorthogonality of the impulse responses. Specifically, the Schwarz inequality bounds $|\langle u_{11}|u_{21}\rangle|^2$ from above by $\langle u_{11}|u_{11}\rangle\langle u_{21}|u_{21}\rangle$ when $\cos\theta_{12} = 1$. Not only that, but the effective cosine $\cos\theta_{12}$ between the impulse-response functions is further restricted below $1/\sqrt{2}$ by Eq. (49). Correspondingly, this imposes an upper bound on $\sigma_{\max}(M_{\text{in}})$ and a lower bound on $\sigma_{\min}(M_{\text{in}})$ for fixed values of $2\gamma_e \langle u_{11}|u_{11}\rangle$ and $2\gamma_e \langle u_{21}|u_{21}\rangle$. Then we conclude that the
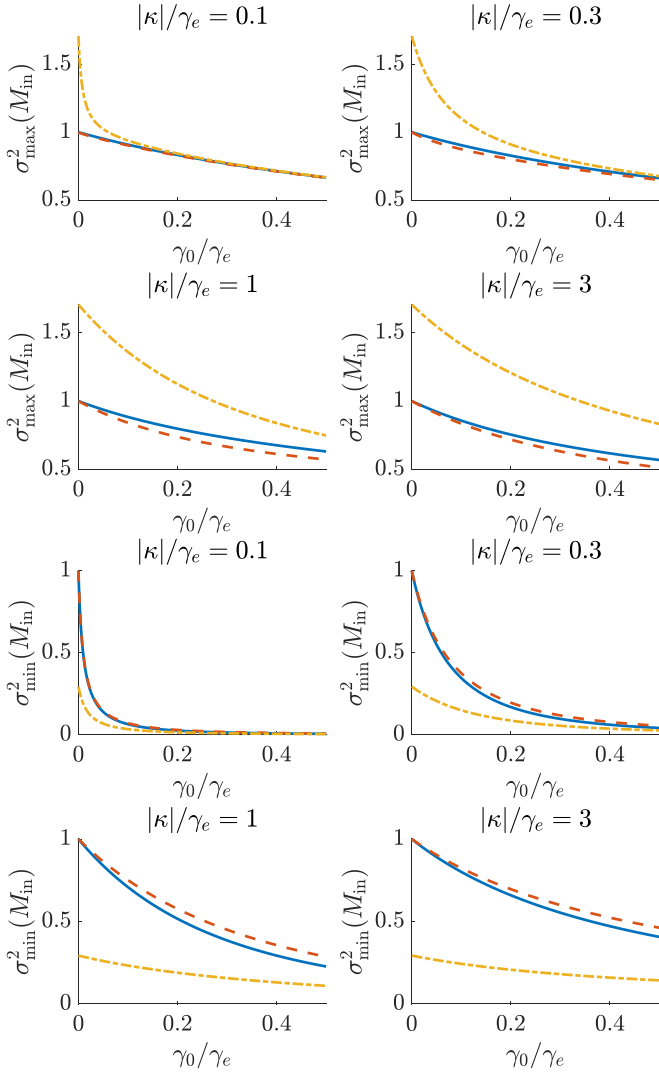
FIG. 4. Plots of $\sigma_{\max}^2(M_{\rm in})$ and its bounds (top), and $\sigma_{\min}^2(M_{\rm in})$ and its bounds (bottom), as functions of γ_0/γ_e and for multiple values of $|\kappa|/\gamma_e$. The squared singular values are shown as solid blue lines; the inner bounds ($2\gamma_e\langle u_{11}|u_{11}\rangle$ and $2\gamma_e\langle u_{21}|u_{21}\rangle$), as a dashed orange lines; and the outer bounds (ρ_-^2 and ρ_+^2) as dotted yellow lines.

singular values $\sigma_j(M_{\rm in})$ are bounded as

$$2\gamma_e\langle u_{11}|u_{11}\rangle \leqslant \sigma_{\max}^2(M_{\rm in}) \leqslant \rho_+^2,$$
$$\rho_-^2 \leqslant \sigma_{\min}^2(M_{\rm in}) \leqslant 2\gamma_e\langle u_{21}|u_{21}\rangle. \quad (53)$$

Here the outer bounds ρ_+ and ρ_-, are given by

$$\frac{\rho_\pm^2}{\gamma_e} = \langle u_{11}|u_{11}\rangle + \langle u_{21}|u_{21}\rangle \pm \sqrt{\langle u_{11}|u_{11}\rangle^2 + \langle u_{21}|u_{21}\rangle^2}.$$
$$(54)$$

In accordance with the previous argument, these are given by substituting $|\langle u_{11}|u_{21}\rangle|^2 = \langle u_{11}|u_{11}\rangle\langle u_{21}|u_{21}\rangle/2$ in the right-hand side of Eq. (52).

We evaluate the singular values $\sigma_j(M_{\rm in})$ of $M_{\rm in}$ and their bounds from Eq. (53) as a function of the normalized intrinsic loss γ_0/γ_e and for different values of the normalized coupling $|\kappa|/\gamma_e$. Our results are shown in Fig. 4. We plot the square of the singular values rather than the singular values directly

because, as discussed in Sec. IV, the latter can be interpreted immediately as the extrema of energy efficiencies.

Several features of Fig. 4 are noteworthy. First, we note that both singular values are exactly equal to unity when $\gamma_0 = 0$, for all values of $|\kappa|/\gamma_e$. This follows because, when $\gamma_0 = 0$, then $2\gamma_e\langle u_{11}|u_{11}\rangle = 2\gamma_e\langle u_{21}|u_{21}\rangle = 1$ and $\langle u_{11}|u_{21}\rangle = 0$, as seen in Fig. 3. Thus, substituting these values into Eq. (52), we get $\sigma_{\max}(M_{\rm in}) = \sigma_{\min}(M_{\rm in}) = 1$. This observation is significant because, as shown in Eqs. (45) and (46), $\sigma_{\max}^2(M_{\rm in})$ and $\sigma_{\min}^2(M_{\rm in})$ are the maximum and minimum of the projected efficiency $\eta_{\rm in}^{(p)}$ over the projected input $|s_{\rm in}^{(p)}(t)\rangle$. Hence, because both are equal to unity when $\gamma_0 = 0$, then $\eta_{\rm in}^{(p)}$ equals unity too for any $|s_{\rm in}^{(p)}(t)\rangle$. Consequently, the input efficiency $\eta_{\rm in} = \eta_{\rm in}^{(p)}\eta_p$ equals the projection efficiency η_p. In other words, when $\gamma_0 = 0$, energy is only lost in the loading process with map $\hat{T}_{\rm in}$ through the projection of the input $|s_{\rm in}(t)\rangle$ into the vector space $\mathcal{V}_{\rm in}$ spanned by $|u_{11}^*(t_m - t)\rangle$ and $|u_{21}^*(t_m - t)\rangle$.

Analogously, because $M_{\rm in}$ and $M_{\rm out}$ have identical singular values [as stated in Eq. (51)], it follows too from Eqs. (45) and (46) that $\eta_{\rm out} = 1$ for $\gamma_0 = 0$, independently of the ring-amplitude vector $a(t_m)$ at the time of modulation. Therefore, no energy is lost in the unloading process with map $\hat{T}_{\rm out}$ in this idealized case.

As γ_0/γ_e increases, both singular values decrease from unity, for all values of $|\kappa|/\gamma_e$ in Fig. 4. Naturally, this reflects that, for nonzero γ_0, it becomes impossible to couple all the input energy into the two-ring system, regardless of input pulse shape. Because of the equality of singular values in Eq. (51), this means too that extraction of the energy from the rings into the bus after AFC becomes increasingly lossy, regardless of the form of $a(t_m)$.

In Fig. 4 the squared singular values remain closer to their inner bounds, $2\gamma_e\langle u_{11}|u_{11}\rangle$ and $2\gamma_e\langle u_{21}|u_{21}\rangle$, than to the outer bounds, $\rho_\pm^2$. Based on Eq. (52) and this section's discussion, this is because the effective cosine $\cos\theta_{12}$ between $u_{11}(t, \Delta)$ and $u_{21}(t, \Delta)$ is small compared to its limit of $1/\sqrt{2}$ over the considered values of γ_0/γ_e and $|\kappa|/\gamma_e$. Note that, according to Fig. 3, $\cos\theta_{12}$ increases faster with γ_0/γ_e for lower $|\kappa|/\gamma_e$. Hence, the singular values in Fig. 4 should deviate from their inner bounds more rapidly with decreasing $|\kappa|/\gamma_e$. However, this is hard to appreciate in Fig. 4, because in this case, the inner and outer bounds grow closer together as well.

Next, we examine the dependence the singular vectors of $M_{\rm in}$ and $M_{\rm out}$ on the rings' TCMT parameters. However, rather than analyzing the components of the singular vectors directly, we analyze the components of their associated Bloch vectors, i.e., their pseudospin vectors [38,59] (or their normalized Stokes parameters, in the context of polarization optics [60–62]). This Bloch vector representation is valid because, for our two-ring AFC, right and left singular vectors are represented by normalized column vectors in $\mathbb{C}^2$; a vector space isomorphic to the state space of a quantum-mechanical two-level system.

Two general advantages of this representation are that the Bloch vector components (or Bloch components for short) are real-valued quantities and that they have an intuitive geometrical interpretation. Additionally, for our particular analysis, we find below that some Bloch components have simple dependences on the impulse-response inner products and the

ring parameters. There is a disadvantage of the representation of singular vectors through their Bloch components. This is that the value of the phase between a matrix's right singular vector and its corresponding left singular vector is lost [60,62]. This phase could be measured by interferometry of the output signal $s_{\text{out}}(t)$, but it does not impact our investigation of AFC efficiency.

Let $S_j^{(r)}(M_{\text{in}})$ be the jth ($j = 1, 2, 3$) Bloch components of the right singular vector of M_{in} corresponding to $\sigma_{\max}(M_{\text{in}})$. Analogously, $S_j^{(l)}(M_{\text{in}})$ is the jth Bloch component of the left singular vector of M_{out} corresponding to $\sigma_{\max}(M_{\text{in}})$; $S_j^{(r)}(M_{\text{out}})$, that of the right singular vector corresponding to $\sigma_{\max}(M_{\text{out}})$; and $S_j^{(l)}(M_{\text{out}})$, that of the left singular vector corresponding to $\sigma_{\max}(M_{\text{out}})$. We need only consider the Bloch components of the singular vectors corresponding to one singular value, because the right singular vectors and left singular vectors are orthogonal sets. Therefore, the Bloch components of the ignored left or right singular vector are the negative of the other left or right singular vector.

With these definitions, the Bloch components $S_j^{(r)}(M_{\text{in}})$ are given by $S_j^{(r)}(M_{\text{in}}) = v_k^\dagger s_j v_k$. Here v_k is the right singular vector of M_{in} associated with $\sigma_{\max}(M_{\text{in}})$, and s_j are the Pauli matrices

$$s_1 = \begin{pmatrix} 0 & 1 \\ 1 & 0 \end{pmatrix}, \quad s_2 = \begin{pmatrix} 0 & -i \\ i & 0 \end{pmatrix}, \quad s_3 = \begin{pmatrix} 1 & 0 \\ 0 & -1 \end{pmatrix}. \tag{55}$$

In Appendix C we show that $S_j^{(l)}(M_{\text{in}})$ and $S_j^{(r)}(M_{\text{out}})$ have particularly simple expressions in terms of the impulse-response inner products and of the ring parameters. Specifically, these are

$$S_1^{(l)}(M_{\text{in}}) = F\text{Re}\{\langle u_{11}|u_{21}\rangle\} = \text{Im}\{\kappa\}/\sqrt{|\kappa|^2 + \bar{\gamma}^2},$$
$$S_2^{(l)}(M_{\text{in}}) = F\text{Im}\{\langle u_{11}|u_{21}\rangle\} = \text{Re}\{\kappa\}/\sqrt{|\kappa|^2 + \bar{\gamma}^2},$$
$$S_3^{(l)}(M_{\text{in}}) = F(\langle u_{11}|u_{11}\rangle - \langle u_{21}|u_{21}\rangle)/2,$$
$$= \bar{\gamma}/\sqrt{|\kappa|^2 + \bar{\gamma}^2} \tag{56}$$

and by

$$S_1^{(r)}(M_{\text{out}}) = F\text{Re}\{\langle u_{12}|u_{11}\rangle\} = -\text{Im}\{\kappa\}/\sqrt{|\kappa|^2 + \bar{\gamma}^2},$$
$$S_2^{(r)}(M_{\text{out}}) = F\text{Im}\{\langle u_{12}|u_{11}\rangle\} = -\text{Re}\{\kappa\}/\sqrt{|\kappa|^2 + \bar{\gamma}^2},$$
$$S_3^{(r)}(M_{\text{out}}) = F(\langle u_{11}|u_{11}\rangle - \langle u_{12}|u_{12}\rangle)/2,$$
$$= \bar{\gamma}/\sqrt{|\kappa|^2 + \bar{\gamma}^2}. \tag{57}$$

In Eqs. (56) and (57), F is a normalization factor that ensures the magnitude of the Bloch vector is unity. Thus, it defined so $F^{-2} = (\langle u_{11}|u_{11}\rangle - \langle u_{21}|u_{21}\rangle)^2/4 + |\langle u_{11}|u_{11}\rangle\langle u_{21}|u_{21}\rangle|^2$. As in Appendix A, $\bar{\gamma} = (\gamma_1 + \gamma_2)/2$ is the ring-averaged decay rate. Equations (56) and (57) hold only if γ_0 is nonzero. Otherwise, $\langle u_{11}|u_{11}\rangle = \langle u_{12}|u_{12}\rangle$ and $\langle u_{11}|u_{12}\rangle = 0$. So the singular values are no longer distinct, according to Eq. (52), and the singular vectors are no longer uniquely defined (up to phase factors), as discussed in Sec. IV.

From Eqs. (56) and (57), we make some key observations. For the first of these, we focus on $S_j^{(l)}(M_{\text{in}})$, but analogous conclusions follow for $S_j^{(r)}(M_{\text{out}})$. First, $S_1^{(l)}(M_{\text{in}})$ and $S_2^{(l)}(M_{\text{in}})$ are nonzero only as a consequence of nonorthogonality of

the impulse responses $u_{11}(t, \Delta)$ and $u_{21}(t, \Delta)$. Similarly, $S_3^{(l)}(M_{\text{in}})$ is nonzero due to the disparity between $\langle u_{11}|u_{11}\rangle$ and $\langle u_{21}|u_{21}\rangle$. Moreover, as a consequence of Eq. (50), $S_3^{(l)}(M_{\text{in}}) > 0$. Thus, the quantity $\sqrt{[S_1^{(l)}(M_{\text{in}})]^2 + [S_2^{(l)}(M_{\text{in}})]^2}$ compared to $S_3^{(l)}(M_{\text{in}})$ is a measure of the impulse-response nonorthogonality relative to the squared-norm difference $(\langle u_{11}|u_{11}\rangle - \langle u_{21}|u_{21}\rangle)$. Although decreasing $|\kappa|$ for fixed γ_e and γ_0 increases the nonorthogonality, as measured by $\cos\theta_{12}$ in Fig. 3, this also increases the difference $(\langle u_{11}|u_{11}\rangle - \langle u_{21}|u_{21}\rangle)$, yielding an overall increase in $S_3^{(l)}(M_{\text{in}})$ and a decrease in magnitude of $S_1^{(l)}(M_{\text{in}})$ and $S_2^{(l)}(M_{\text{in}})$, as indicated by the rightmost side of Eqs. (56) and (57).

The second observation is that, for any set of ring parameters excluding $\gamma_0 = 0$,

$$S_1^{(l)}(M_{\text{in}}) = -S_1^{(r)}(M_{\text{out}}),$$
$$S_2^{(l)}(M_{\text{in}}) = -S_2^{(r)}(M_{\text{out}}),$$
$$S_3^{(l)}(M_{\text{in}}) = S_3^{(r)}(M_{\text{out}}). \tag{58}$$

Consequently, the left singular vectors of M_{in} approximate the right singular vectors of M_{out} if and only if $S_1^{(l)}(M_{\text{in}})$ and $S_2^{(l)}(M_{\text{in}})$ are close to zero. From Eqs. (56) and (57), this occurs if and only if

$$|\kappa| \ll \bar{\gamma}. \tag{59}$$

This observation is significant because the similarity between the left singular vectors of M_{in} and the right singular vectors of M_{out} influences the singular values of their product, M, the matrix representing the overall AFC process. This is discussed below in Sec. VII and in Appendix D.

The analogs of Eqs. (56) and (57) for $S_j^{(r)}(M_{\text{in}})$ and $S_j^{(l)}(M_{\text{out}})$ are generally complicated and yield little insight. Thus, we omit their general discussion and mostly investigate $S_j^{(r)}(M_{\text{in}})$ and $S_j^{(l)}(M_{\text{out}})$ numerically. This discrepancy in the complexity of $S_j^{(r)}(M_{\text{in}})$ and $S_j^{(l)}(M_{\text{out}})$ compared to that of $S_j^{(l)}(M_{\text{in}})$ and $S_j^{(r)}(M_{\text{out}})$ arises because the components of the right singular vectors of M_{in} and the left singular vectors M_{out} depend on the orthonormal basis chosen for $\mathcal{V}_{\text{in}}$ and $\mathcal{V}_{\text{out}}$. In contrast, the left singular vectors of M_{in} and the right singular vectors of M_{out} have a natural basis as column vectors of energy amplitudes in Ring 1 and Ring 2.

There is one analytical property of the Bloch components $S_j^{(r)}(M_{\text{in}})$ and $S_j^{(l)}(M_{\text{out}})$ that we derive in Appendix C, and that is useful to point out. This is that, just as $S_j^{(l)}(M_{\text{in}})$ and $S_j^{(r)}(M_{\text{out}})$ satisfy Eq. (58), $S_j^{(r)}(M_{\text{in}})$ and $S_j^{(l)}(M_{\text{out}})$ obey the relation

$$S_1^{(r)}(M_{\text{in}}) = -S_1^{(l)}(M_{\text{out}}),$$
$$S_2^{(r)}(M_{\text{in}}) = -S_2^{(l)}(M_{\text{out}}),$$
$$S_3^{(r)}(M_{\text{in}}) = S_3^{(l)}(M_{\text{out}}), \tag{60}$$

valid for any set of ring parameters, except for $\gamma_0 = 0$ when the singular values M_{in} and M_{out} become degenerate. Unlike Eq. (58), Eq. (60) holds only for our choice of bases $\{|n_1^{(\text{in})}\rangle, |n_2^{(\text{in})}\rangle\}$ for $\mathcal{V}_{\text{in}}$, and $\{|n_1^{(\text{out})}\rangle, |n_2^{(\text{out})}\rangle\}$ for $\mathcal{V}_{\text{out}}$ that

satisfy Eq. (38). If either of these were changed, Eq. (58) would still hold, but Eq. (60) would not in general.

Next, we study numerically the dependence of the complete SVD, both singular values and singular vectors, of M_{in} on the ring parameters. As a consequence of Eqs. (51), (58), and (60), this analysis covers the SVD of M_{out} as well. In Fig. 5 we plot as functions of γ_0/γ_e and for various different $|\kappa|/\gamma_e$ the squared singular values $\sigma_{\max}^2(M_{\text{in}})$ and $\sigma_{\min}^2(M_{\text{in}})$, along with the Bloch components $S_2^{(r)}(M_{\text{in}})$, $S_3^{(l)}(M_{\text{in}})$, $S_2^{(r)}(M_{\text{in}})$, and $S_3^{(l)}(M_{\text{in}})$. The components $S_1^{(r)}(M_{\text{in}})$ and $S_1^{(l)}(M_{\text{in}})$ are omitted because they are always zero. This is a consequence of our choice of taking the interring coupling coefficient κ to be real and positive.

From Fig. 5, we first examine the behavior of the singular values $\sigma_{\max}(M_{\text{in}})$ and $\sigma_{\min}(M_{\text{in}})$. As seen in Fig. 4, they both start at unity for $\gamma_0 = 0$ and then decrease with increasing γ_0/γ_e for all values of $|\kappa|/\gamma_e$. In contrast to Fig. 4, in Fig. 5 the effect on $\sigma_{\max}(M_{\text{in}})$ and $\sigma_{\min}(M_{\text{in}})$ of varying $|\kappa|/\gamma_e$ is more transparent. For fixed γ_0/γ_e, increasing $|\kappa|/\gamma_e$ simultaneously decreases $\sigma_{\max}(M_{\text{in}})$ and increases $\sigma_{\min}(M_{\text{in}})$. Furthermore, this increment and this decrement are such that, in the limit of $|\kappa| \rightarrow \infty$ and for fixed γ_0/γ_e, $\sigma_{\max}(M_{\text{in}})$ and $\sigma_{\min}(M_{\text{in}})$ converge to a common value. As seen in Fig. 3, increasing $|\kappa|/\gamma_e$ inhibits impulse-response nonorthogonality, i.e., $\cos\theta_{12}$. So this convergence of $\sigma_{\max}(M_{\text{in}})$ and $\sigma_{\min}(M_{\text{in}})$ for increasing $|\kappa|/\gamma_e$ can be understood as a convergence of $2\gamma_e\langle u_{11}|u_{11}\rangle$ and $2\gamma_e\langle u_{21}|u_{21}\rangle$ to a common value. By manipulation of the formulas in Appendix A for $\langle u_{11}|u_{11}\rangle$ and $\langle u_{21}|u_{21}\rangle$, it is straightforward to verify that this common asymptote is given by

$$\lim_{|\kappa|\rightarrow\infty}\sigma_{\max}^2(M_{\text{in}}) = \lim_{|\kappa|\rightarrow\infty}\sigma_{\min}^2(M_{\text{in}}) = \frac{\gamma_e}{\gamma_1+\gamma_2}, \qquad (61)$$

assuming that both γ_0 and γ_e remain finite in this limit. Likewise, it is easy to verify that, for vanishing $|\kappa|$,

$$\sigma_{\max}^2(M_{\text{in}}) = \gamma_e/\gamma_1, \quad \sigma_{\min}^2(M_{\text{out}}) = 0. \qquad (62)$$

This value of $\sigma_{\max}^2(M_{\text{in}})$ for $|\kappa| = 0$ then equals the Schwarz limit for the loading of a single ring resonator [28], as one might expect. Similarly, it is intuitively clear that for zero interring coupling, the minimum singular value corresponds to the efficiency of loading the now-uncoupled Ring 2 and thus equals zero.

Next, we inspect the plots for the Bloch components $S_2^{(l)}(M_{\text{in}})$ and $S_3^{(l)}(M_{\text{in}})$ of the left singular vectors of M_{in}. In Fig. 5 we see that their behavior is well described by the expressions in the rightmost side of Eq. (56). $S_2^{(l)}(M_{\text{in}})$ increases with $|\kappa|/\gamma_e$ and decreases with γ_0/γ_e; while $S_3^{(l)}(M_{\text{in}})$ decreases with $|\kappa|/\gamma_e$ and increases with γ_0/γ_e, ensuring that the Bloch vector remains normalized.

The behavior of $S_2^{(r)}(M_{\text{in}})$ and $S_3^{(r)}(M_{\text{in}})$, corresponding to the right singular vectors of M_{in}, is slightly different. For fixed γ_0/γ_e and increasing $|\kappa|/\gamma_e$, $S_2^{(r)}(M_{\text{in}})$ increases and $S_3^{(r)}(M_{\text{in}})$ decreases, just like $S_2^{(l)}(M_{\text{in}})$ and $S_3^{(l)}(M_{\text{in}})$, respectively. However, $S_2(M_{\text{in}})$ increases and $S_3(M_{\text{in}})$ decreases for increasing γ_0/γ_e and fixed $|\kappa|/\gamma_e$. In contrast, $S_2^{(l)}(M_{\text{in}})$ and $S_3^{(l)}(M_{\text{in}})$ exhibit the opposite behavior in this case.
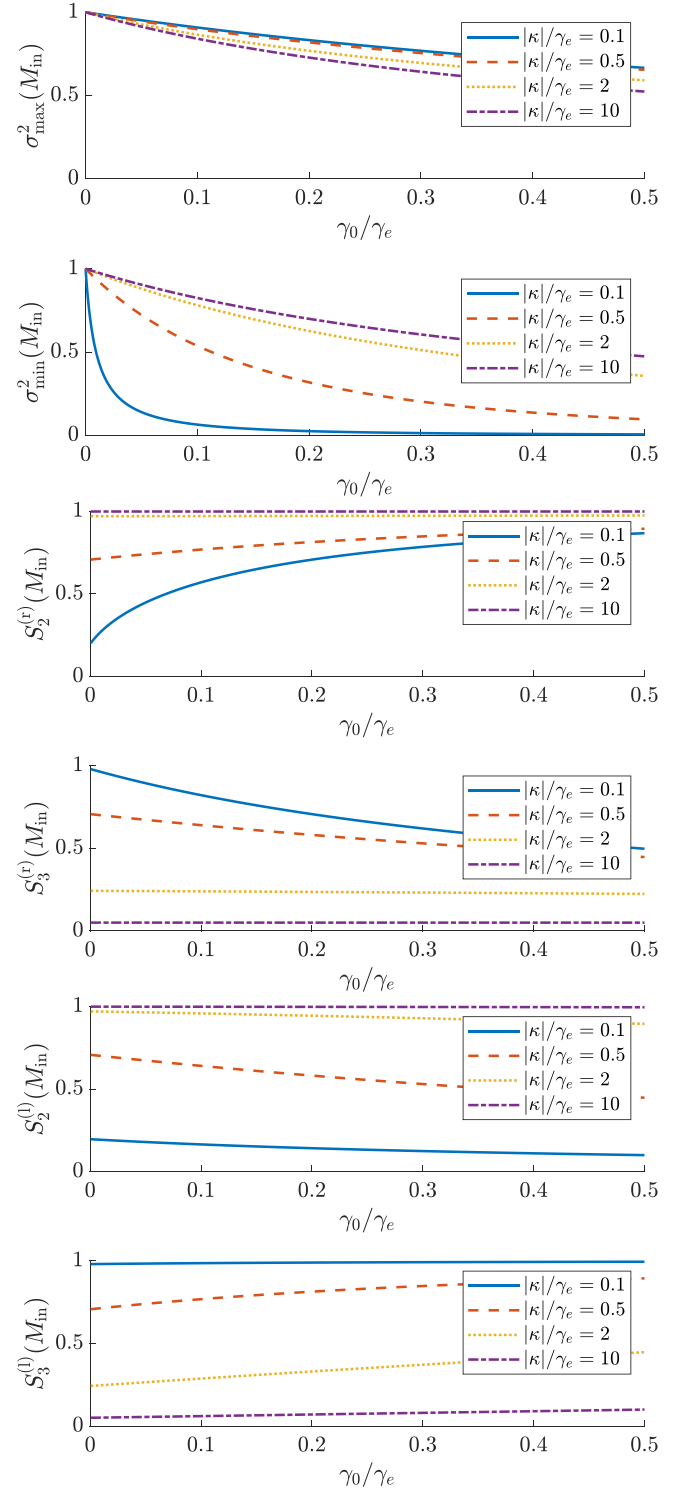

FIG. 5. Singular value decomposition of M_{in} as a function of γ_0/γ_e and for different values of $|\kappa|/\gamma_e$.

VII. NUMERICAL SVD OF THE AFC OPERATOR

Having studied in detail the SVD of M_{in} and M_{out} in Sec. VI, we now examine the SVD of their product, M, the matrix representing the full AFC linear operator. Because the expression for M is given by the product of those for M_{in} and M_{out}, it is complicated. Hence, an explicit analytical SVD
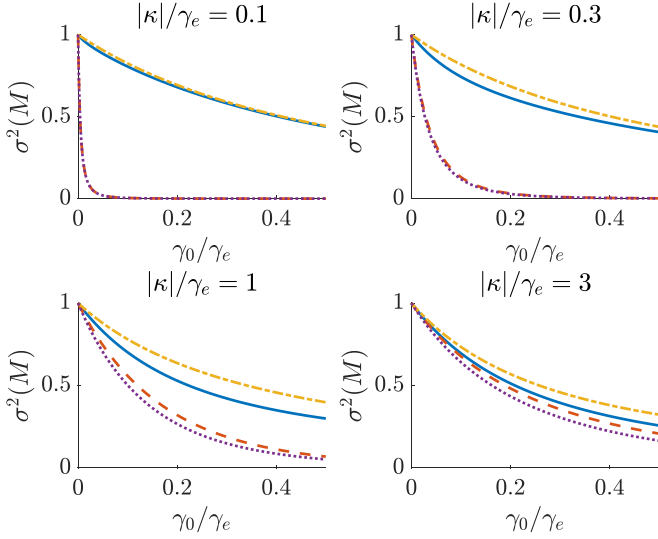
FIG. 6. Squared singular values of M and their bounds as functions of γ_e/γ_0 and for various values of $|\kappa|/\gamma_e$. $\sigma_{\max}^2(M)$ is shown as a solid blue line; $\sigma_{\min}^2(M)$, as a dashed orange line; the upper bound $\sigma_{\max}^2(M_{\mathrm{in}})\sigma_{\max}^2(M_{\mathrm{out}})$, as a dotted yellow line; and the lower bound $\sigma_{\min}^2(M_{\mathrm{in}})\sigma_{\min}^2(M_{\mathrm{out}})$, as a dashed-dotted purple line.

of M yields unwieldy mathematical expressions and little physical insight. Thus, we investigate the SVD of M mostly numerically.

Still, we show in Appendix D that the fact that M equals the product of M_{in} and M_{out} allows us to bound its singular values in terms of those of M_{in} and M_{out}. Thus, we obtain

$$\sigma_{\max}(M) \leqslant \sigma_{\max}(M_{\mathrm{in}})\sigma_{\max}(M_{\mathrm{out}}),$$
$$\sigma_{\min}(M) \geqslant \sigma_{\min}(M_{\mathrm{in}})\sigma_{\min}(M_{\mathrm{out}}). \tag{63}$$

Because the singular values of M_{in} equal those of M_{out}, as established in Appendix C, the terms on the right-hand side of Eq. (63) can also be written as $\sigma_{\max}^2(M_{\mathrm{in}})$ and $\sigma_{\min}^2(M_{\mathrm{in}})$ or as $\sigma_{\max}^2(M_{\mathrm{out}})$ and $\sigma_{\min}^2(M_{\mathrm{out}})$. Additionally, we show in Appendix D that a sufficient condition to achieve equality in both lines of Eq. (63) is for the left singular vectors of M_{in} to equal the right singular vectors of M_{out}. Accordingly, we expect that differences between these sets of singular vectors will cause $\sigma_{\max}(M)$ to decrease below its upper bound of $\sigma_{\max}(M_{\mathrm{in}})\sigma_{\max}(M_{\mathrm{out}})$, and $\sigma_{\min}(M)$ to increase above its lower bound of $\sigma_{\min}(M_{\mathrm{in}})\sigma(M_{\mathrm{out}})$.

To verify Eq. (63) and determine its implications, we compute the squared singular values of M_{in} and plot them alongside their corresponding bounds for different values of the ring parameters. The resulting plots are shown in Fig. 6. Two features of these plots are noteworthy. First, both $\sigma_{\max}^2(M)$ and $\sigma_{\min}^2(M)$ indeed lie below the upper bound $\sigma_{\max}^2(M_{\mathrm{in}})\sigma_{\max}^2(M_{\mathrm{out}})$ and above the lower bound $\sigma_{\min}^2(M_{\mathrm{in}})\sigma_{\min}^2(M_{\mathrm{out}})$ for all considered values of γ_0/γ_e and $|\kappa|/\gamma_e$. This confirms the validity of the analytically derived Eq. (63). Second, as $|\kappa|/\gamma_e$ is increased, the singular values $\sigma_{\max}(M)$ and $\sigma_{\min}(M)$ grow closer to each other, as do their lower and upper bounds. Of course, in the case of the upper and lower bounds, this follows from the fact that $\sigma_{\max}(M_{\mathrm{in}})$ and $\sigma_{\min}(M_{\mathrm{in}})$ exhibit this same behavior in Fig. 5.

Moreover, we observe that for small $|\kappa|/\gamma_e$, $\sigma_{\max}(M)$ and $\sigma_{\min}(M)$ lie close to their outer bounds. Then, as $|\kappa|/\gamma_e$ is increased, they grow apart from them. But, then, this separation is inhibited by the outer bounds growing closer themselves. As stated above and discussed in Appendix D, the decrease of $\sigma_{\max}(M)$ below $\sigma_{\max}(M_{\mathrm{in}})\sigma_{\max}(M_{\mathrm{out}})$ [and the increase of $\sigma_{\min}(M)$ above $\sigma_{\min}(M_{\mathrm{in}})\sigma_{\min}(M_{\mathrm{out}})$] is a consequence of the mismatch between the left singular vectors of M_{in} and the right singular vectors of M_{out}. From Eqs. (56) and (57), we find that this mismatch increases with $|\kappa|/\gamma_e$ for fixed γ_0/γ_e. This explains the increasing deviation of the $\sigma_{\max}(M)$ and $\sigma_{\min}(M)$ from their bounds, as $|\kappa|/\gamma_e$ increments.

As in Sec. VI, both singular values of M are equal to unity when γ_0 vanishes, regardless of the value of $|\kappa|/\gamma_e$. This implies that for $\gamma_0 = 0$ the projected AFC efficiency, $\eta^{(p)}$, equals unity for any form of the projected input $|s_{\mathrm{in}}^{(p)}(t)\rangle$. In this case it follows from Eq. (34) that $\eta = \eta_p$. In other words, the AFC efficiency equals the projection efficiency. Hence, in this ideal case, energy is only lost in AFC through the projection of $|s_{\mathrm{in}}(t)\rangle$ into $\mathcal{V}_{\mathrm{in}}$ spanned by $|u_{11}^*(t_m - t)\rangle$ and $|u_{21}^*(t_m - t)\rangle$. As γ_0 increases from zero, $\sigma_{\max}(M)$ and $\sigma_{\min}(M)$ decrease below unity, so the map from the projected input $|s_{\mathrm{in}}^{(p)}(t)\rangle$ to $|s_{\mathrm{out}}(t)\rangle$ becomes lossy.

Next, we investigate numerically the full SVD of the AFC matrix M as a function of the ring parameters. Thus, as in Fig. 5, we plot $\sigma_{\max}^2(M)$, $\sigma_{\min}^2(M)$, $S_2^{(r)}(M)$, $S_3^{(r)}(M)$, $S_2^{(l)}(M)$, and $S_3^{(l)}(M)$ as functions of γ_0/γ_e and for different values of $|\kappa|/\gamma_e$ in Fig. 7. As in Fig. 5, we omit the Bloch components $S_1^{(r)}(M)$ and $S_1^{(l)}(M)$ because they vanish for all ring parameters as a consequence of setting κ as real valued.

Just like $\sigma_{\max}(M_{\mathrm{in}})$ and $\sigma_{\min}(M_{\mathrm{in}})$ in Fig. 5, it is evident in Fig. 7 that $\sigma_{\max}(M)$ and $\sigma_{\min}(M)$ grow closer as $|\kappa|/\gamma_e$ is increased. This occurs because their outer bounds from Eq. (63) themselves grow closer, as discussed in Sec. VI, thus forcing $\sigma_{\max}(M)$ and $\sigma_{\min}(M)$ to converge to a common value. From this argument and from Eq. (61), it follows that the common asymptote for $\sigma_{\max}^2(M)$ and $\sigma_{\min}^2(M)$ is given by

$$\lim_{|\kappa| \to \infty} \sigma_{\max}^2(M) = \lim_{|\kappa| \to \infty} \sigma_{\min}^2(M) = \left(\frac{\gamma_e}{\gamma_1 + \gamma_2}\right)^2. \tag{64}$$

As for Eq. (61), we assume for Eq. (64) that both γ_e and γ_0 remain finite.

From Fig. 7, it is also apparent that $\sigma_{\max}(M)$ and $\sigma_{\min}(M)$ each converge to distinct curves as $|\kappa|$ tends to zero. To determine their values for $|\kappa| = 0$, we recall that the inequalities in Eq. (63) become equalities when the left singular vectors of M_{in} equal the right singular vectors of M_{out}. And from Eqs. (56) and (57), this is the case when $|\kappa| = 0$. Then we may substitute Eq. (62) into Eq. (63), now equalities, to obtain

$$\sigma_{\max}^2(M) = (\gamma_e/\gamma_1)^2, \quad \sigma_{\min}^2(M) = 0, \tag{65}$$

for $|\kappa| = 0$. As in Eq. (62), Eq. (65) has an intuitive interpretation. The first line of Eq. (65) means that for zero interring coupling, AFC in the two-ring system is just as efficient as AFC in a single ring (Ring 1) [28]. The second line means that for zero interring coupling, the efficiency of AFC in Ring 2 equals zero.

Next, we discuss the Bloch components in Fig. 7. Their dependence on the ring parameters is noticeably different from
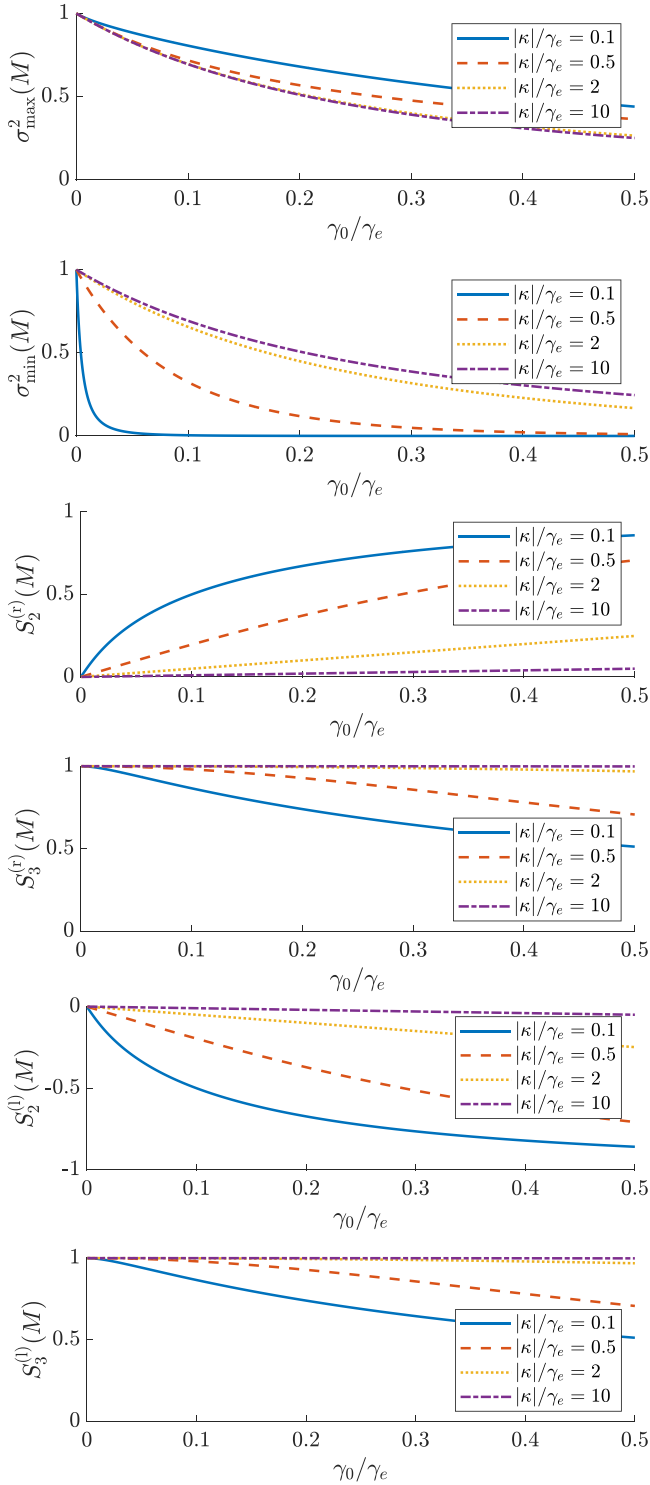
FIG. 7. Singular value decomposition of M as a function of γ_0/γ_e and for different values of $|\kappa|/\gamma_e$.

those in Fig. 5. For decreasing γ_0/γ_e, $S_2^{(r)}(M)$ and $S_2^{(l)}(M)$ always converge to zero, and $S_3^{(r)}(M)$ and $S_3^{(l)}(M)$ always converge to unity. In contrast, in Fig. 5 they can take any value between 0 and 1 as γ_0/γ_e converges to zero, depending on the value of $|\kappa|/\gamma_e$. Additionally, the rate at which $S_3^{(r)}(M)$ and $S_3^{(l)}(M)$ decrease from unity as γ_0/γ_e increases from zero in

Fig. 7 clearly decreases with increasing $|\kappa|/\gamma_e$. Correspondingly, the rate at which $S_2^{(r)}(M)$ and $S_2^{(l)}(M)$ grow in magnitude with increasing γ_0/γ_e decreases with $|\kappa|/\gamma_0$ as well. This is required for the Bloch vectors to remain normalized. Finally, for the range of ring parameters in Fig. 7, the Bloch components appear to satisfy

$$S_2^{(r)}(M) = -S_2^{(l)}(M), \quad S_3^{(r)}(M) = S_3^{(l)}(M), \qquad (66)$$

analogous to Eqs. (58) and (60). However, the validity of Eq. (66) is harder to verify analytically due to the explicit expression for M being considerably more unwieldy that of M_{in}.

VIII. EFFICIENCY ANALYSIS OF AFC OF A SYMMETRIC SINGLE-LOBE PULSE

In this section we examine the AFC of an input pulse of fixed shape and duration in the two-ring system of Fig. 1. We investigate and optimize this process's efficiency with respect to the rings' TCMT parameters. We use the formalism developed in Secs. III to VII to interpret our results.

For the pulse shape of the AFC input $s_{in}(t)$, we follow Ref. [28] and consider a raised-cosine pulse, also known as a Hann function in numerical Fourier analysis [63,64]. Thus, $s_{in}(t)$ is given by

$$s_{in}(t) = \sqrt{\frac{2E_{in}}{3\tau}}[1 + \cos(2\pi t/\tau)]\exp(-i\omega_0 t)$$
$$\times [\Theta(t + \tau/2) - \Theta(t - \tau/2)]. \qquad (67)$$

Here $E_{in} = \langle s_{in}(t)|s_{in}(t)\rangle$ is the input energy, and τ, the input pulse duration. As in Sec. II, ω_0 is the rings' original bare resonance frequency, and $\Theta(t)$, the Heaviside step function. The total duration τ is related to the pulse's root mean square duration τ_{RMS} via $\tau_{RMS} \approx 0.141\tau$ [28]. We choose the raised-cosine pulse shape because it is a symmetric, single-lobe shape, which is usually of interest in optical telecommunications [5,36]. Additionally, this shape has a finite support, i.e., it is nonzero only over a finite time interval, unlike the typically analyzed Gaussian envelope. This latter feature simplifies the numerical analysis and optimization of its AFC. Moreover, as we show later in this section, the AFC efficiency of this raised-cosine input is mostly determined by the symmetry and single-lobe nature of the pulse. Hence, the analysis for the AFC optimization of a raised-cosine input applies qualitatively and yields similar results for other symmetric, single-lobe pulse shapes, e.g., Gaussian, super-Gaussian, and hyperbolic secant.

We aim to determine the upper limit to the AFC efficiency of the raised-cosine pulse and to observe how this efficiency decreases with increasing intrinsic ring loss γ_0. To do so, we first solve numerically the TCMT equations for the ring amplitudes at the time of modulation $a(t_m)$ and compute the corresponding AFC efficiency for $\gamma_0 = 0$ and a broad range of ring parameters and modulation times. Then we compare the obtained AFC efficiencies to estimate the ring parameters for global maximum efficiency. Subsequently, we refine this estimate via numerical local optimization.

In this way we find that the maximum AFC efficiency η of a raised-cosine pulse for $\gamma_0 = 0$ is of 0.9683. This maximum

is achieved when $t_m = 0.3280\tau$, $\gamma_e = 5.5324\tau^{-1}$, and $|\kappa| = 4.4027\tau^{-1}$. Qualitatively, then the conditions for optimal AFC of the raised-cosine pulse are as follows. The intrinsic decay rate γ_0 must be small compared to the extrinsic decay rate γ_0, and the input pulse's bandwidth $\sim\tau^{-1}$. The external decay rate γ_e must be moderately large compared to the input bandwidth $\sim\tau^{-1}$. The interring coupling must be slightly underdamped by the extrinsic decay. Finally, the ring modulation must be applied at a time t_m slightly after the input's maximum relative to the pulse's root mean square duration. The maximum AFC efficiency of 0.9683 in our two-ring system is appreciably larger than the single-ring maximum AFC efficiency of 0.7951 found in Ref. [28] for the same raised-cosine envelope.

To explain this difference in efficiencies, we recall from Sec. VII and Ref. [28], that for $\gamma_0 = 0$, the overall AFC efficiency η equals the projection efficiency η_p, for both the two-ring system and for a single-ring system. From Eq. (29), we recall that the projection efficiency is simply the ratio of the energy in the projected input $|s_{\text{in}}^{(p)}(t)\rangle$ to that in the overall input $|s_{\text{in}}(t)\rangle$. Therefore, a larger AFC efficiency in the two-ring system than in the single-ring system means that the $s_{\text{in}}(t)$ in Eq. (67) achieves a larger projection in the input space $\mathcal{V}_{\text{in}}$ of the two-ring system than that of the single-ring system.

The main reason why the raised-cosine input $s_{\text{in}}(t)$ achieves a greater projection into $\mathcal{V}_{\text{in}}$ of the two-ring system than that of the single-ring system is the shape of the Ring 2's impulse response envelope, $\bar{u}_{21}(t)$, shown in Fig. 2. As discussed in Sec. V, $\bar{u}_{21}(t)$ is continuous at $t = 0$, and, if $\gamma_e \gtrsim |\kappa|$, most of the squared norm $\langle\bar{u}_{21}(t)|\bar{u}_{21}(t)\rangle$ is accumulated under the first peak after $t = 0$. Thus, the time-reversed impulse response $u_{21}^*(t_m - t, 0)$ can match closely the raised-cosine input $s_{\text{in}}(t)$. This contrasts with the single-ring case, where its impulse response is a discontinuous, truncated, decaying exponential. Hence, the maximum overlap between the raised-cosine $s_{\text{in}}(t)$ and the single-ring time-reversed impulse response is poor, which limits the AFC efficiency to the aforementioned value of 0.7951.

To illustrate this interpretation, we examine Fig. 8. In it we display two plots. The first pertains to the optimized single-ring AFC of the raised-cosine input $s_{\text{in}}(t)$ for $\gamma_0 = 0$. This first plot shows the envelopes of: $s_{\text{in}}(t)$, its projection $s_{\text{in}}^{(p)}(t)$ into the ring's impulse response for optimal AFC, and the corresponding AFC output $s_{\text{out}}(t)$. Analogously, the second plot pertains to the optimized two-ring AFC of the same input $s_{\text{in}}(t)$. It shows the envelopes of: $s_{\text{in}}(t)$, its projection $s_{\text{in}}^{(p)}(t)$ into $\mathcal{V}_{\text{in}}$, and the corresponding AFC output $s_{\text{out}}(t)$. By comparing these two plots, it is clear that $s_{\text{in}}^{(p)}(t)$ of the two-ring system matches more closely $s_{\text{in}}(t)$ than that of the single-ring system. Consequently, it is expected that the two-ring system conserves more of the energy of $s_{\text{in}}(t)$ upon projection into $s_{\text{in}}^{(p)}(t)$.

For both the single-ring and two-ring system, the envelope of the output $s_{\text{out}}(t)$ seems proportional to the time-reversed envelope of $s_{\text{in}}^{(p)}(t)$ in Fig. 8. For the single-ring system, this apparent time-reversal is exact for $\gamma_0 = 0$ and for any form of $s_{\text{in}}(t)$ and any choice of ring parameters and t_m. However, for the two-ring system, this is only approximately true for
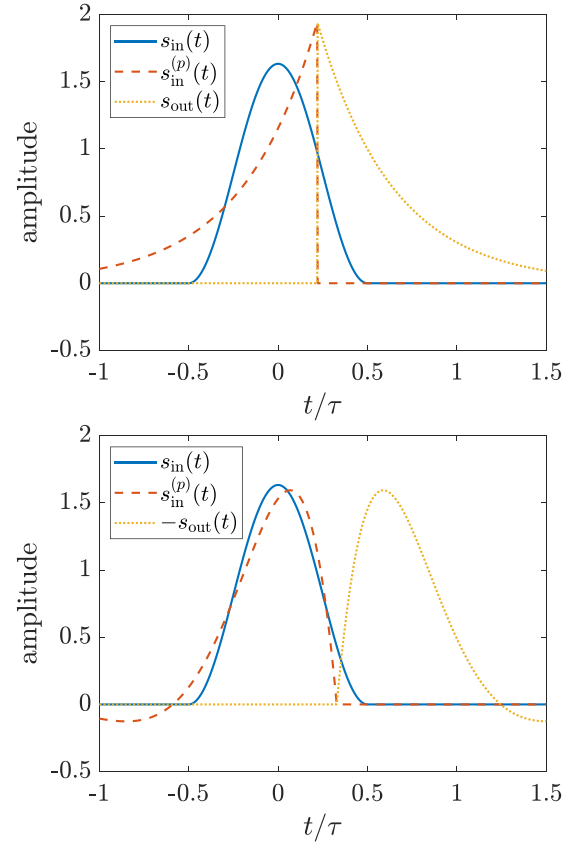

FIG. 8. Envelopes of the raised-cosine input envelope $s_{\text{in}}(t)$, the associated projected input envelope $s_{\text{in}}^{(p)}(t)$, and the associated AFC output envelope $s_{\text{out}}(t)$. The top axis corresponds to single-ring AFC; the bottom axis corresponds to two-ring AFC. Amplitude units are arbitrary.

$\gamma_0 = 0$ if $s_{\text{in}}^{(p)}(t)$ is mostly proportional to either $u_{11}^*(t_m - t, 0)$ or $u_{21}^*(t_m - t, 0)$. This is because the envelope's projection onto $u_{11}^*(t_m - t, 0)$ is only time-reversed when multiplied by $u_{11}(t - t_m, \Delta)$ at the AFC output; but its projection onto $u_{21}^*(t_m - t, 0)$ is time-reversed and multiplied by -1 when multiplied by $u_{12}(t - t_m, \Delta)$.

We observe one last feature of Fig. 8. This is that the frequency-shifted output $s_{\text{out}}(t)$ is noticeably discontinuous at the modulation time t_m in single-ring AFC, but it is seemingly continuous at t_m in two-ring AFC. This occurs because, in two-ring AFC, most of the energy is stored in Ring 2 at t_m, so this energy is released via $u_{12}(t - t_m, \Delta)$, which is continuous at $t = t_m$, as discussed in Sec. V. Similarly, in single-ring AFC, the energy in the single ring is released via the ring's impulse response. In contrast, however, this impulse response is a decaying exponential multiplied by a step function $\Theta(t - t_m)$, and is thus discontinuous at $t = t_m$.

This observation on the continuity of $s_{\text{out}}(t)$ is important because the discontinuities of the AFC's outputs govern the asymptotic behavior of the output spectra and, hence, their robustness to dispersive phenomena (e.g., dispersive propagation and filtering). Let ω be the frequency variable for the spectrum of $s_{\text{out}}(t)$. According to Riemman's lemma [35], the discontinuity of single-ring AFC output $s_{\text{out}}(t)$ at $t = t_m$ implies that its spectrum decays as ω^{-1} for $|\omega| \to \infty$. In
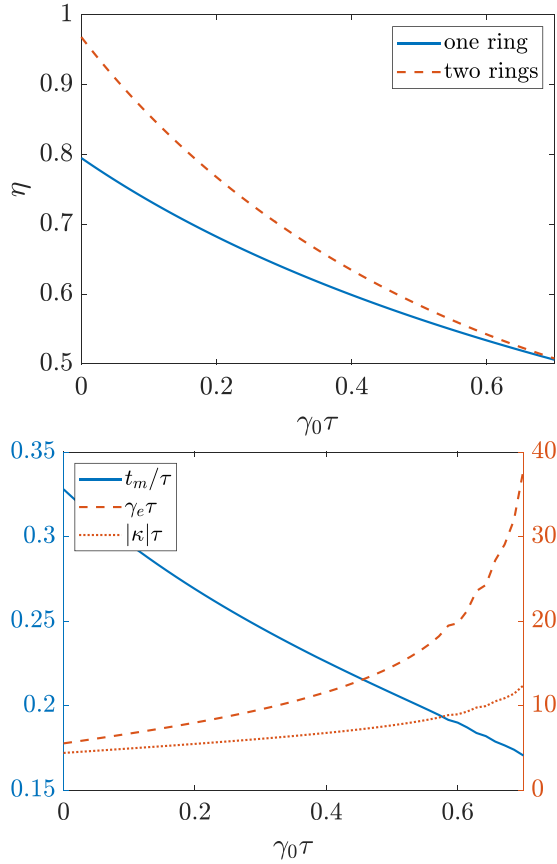
FIG. 9. Maximum efficiency for a raised-cosine input of single-ring AFC and two-ring AFC as functions of intrinsic loss γ_0 (top). Modulation time t_m and ring parameters, γ_e and $|\kappa|$, for optimal two-ring AFC of a raised-cosine input as functions of γ_0 (bottom).

contrast, for two-ring AFC $u_{12}(t, \Delta)$ is continuous, albeit with discontinuous derivative at $t = t_m$ (see Sec. V). Hence, from Riemann's lemma, the spectrum of $u_{12}(t, \Delta)$ decays as ω^{-2} for $|\omega| \to \infty$. Therefore, the output spectrum of two-ring AFC decays more rapidly with ω than that of single-ring AFC, and is consequently more robust to dispersive effects.

Next, we compare how the maximum AFC efficiencies of the raised-cosine input in the single-ring and two-ring system vary as we increase the intrinsic ring loss γ_0. To do this, we use a numerical local optimizer to find how the maximum AFC efficiency and the ring parameters required to attain this maximum are changed as γ_0 is increased. Naturally, the main assumption of this method is that increasing γ_0 only slightly perturbs the configuration for globally optimal AFC for both single-ring and two-ring networks. In Fig. 9 we present our numerical results on the optimization of AFC of the raised-cosine input in both the single-ring and two-ring networks and for increasing γ_0. We report the attained AFC efficiencies in both configurations, along with the required modulation time t_m (referred to the input pulse's peak) and the required ring parameters γ_e and $|\kappa|$ for the two-ring system. The ring parameters and modulation time for optimal AFC in a single-ring system were studied in Ref. [28], so they are omitted for succinctness.

In Fig. 9 we observe that the maximum AFC efficiency of the raised-cosine input is larger in the two-ring system than in the single-ring system for all considered values of γ_0. This is a remarkable result as it implies that the two-ring configuration generally offers a better choice for AFC of symmetric pulses. We explain this with two intuitive arguments. First, as we already noted for $\gamma_0 = 0$, the raised-cosine input achieves a larger projection into the input space $\mathcal{V}_{in}$ of the two-ring system than that of the single-ring system. For $\gamma_0 = 0$, this immediately translates to a larger AFC efficiency. Accordingly, for sufficiently small γ_0, we expect two-ring AFC to continue being more efficient than single-ring AFC. Second, if $|\kappa| = 0$ in two-ring AFC, it clearly acts as single-ring AFC. Therefore, two-ring AFC should, at worst, possess the same efficiency as single-ring AFC, and never lower.

Now, we interpret the variation in Fig. 9 of the modulation time t_m and ring parameters γ_e and $|\kappa|$ for optimal two-ring AFC with increasing γ_0. In Fig. 9 we observe that t_m decreases from 0.3280τ at $\gamma_0 = 0$ to almost 0.15τ at $\gamma_0 = 0.7\tau^{-1}$; γ_e increases from $5.5324\tau^{-1}$ to almost $40\tau^{-1}$; and $|\kappa|$ increases from $4.4027\tau^{-1}$ to barely above $10\tau^{-1}$. This variation in the modulation time and ring parameters with γ_0 is similar to that of the single-ring case [28]. The coupling rate γ_e increases to inhibit energy loss to γ_0 during the loading and unloading processes. Meanwhile, t_m approaches the pulse peak at $t = 0$ to avoid energy leakage due to nonzero γ_0.

Though both γ_e and $|\kappa|$ increase with γ_0 in Fig. 9, they do such that the ratio $\gamma_e/|\kappa|$ increases. This causes inter-ring coupling to transition from underdamped to overdamped. This transition removes the amplitude oscillations of $\bar{u}_{21}(t)$, characteristic of the underdamped regime, and makes $\bar{u}_{21}(t)$ have a common phase for all $t > 0$. This constant phase helps optimize the loading $\hat{T}_{in}$ of the input pulse by ensuring the integrand determining $a_2(t_m)$ are in-phase for a long integration time t and thus interfere constructively.

To understand more deeply our results for optimal AFC of a raised-cosine pulse, we factorize the AFC efficiency η as the product of the projection efficiency η_p and the projection efficiency $\eta^{(p)}$, as in Eq. (34). To do this, we compute η_p from $a(t_m)$ and the ring parameters, as in Appendix B, and then evaluate $\eta^{(p)}$ as the quotient η/η_p. The results are shown in Fig. 10. As argued in the discussion of Fig. 8, when $\gamma_0 = 0$, $\eta^{(p)} = 1$ for both single-ring and two-ring AFC, so $\eta = \eta_p$. As γ_0 increases from zero, $\eta^{(p)}$ and η_p decrease for both ring networks, causing their product, η, to decrease accordingly. For both cases, the projected efficiency $\eta^{(p)}$ decrease similarly, starting at 1 for $\gamma_0 = 0$, and lying close to 0.7 for $\gamma_0 = 0.7\tau^{-1}$.

The main difference in Fig. 10 between single-ring and two-ring AFC clearly lies on their values for the projection efficiency η_p. For single-ring AFC, η_p starts at 0.7951 for $\gamma_0 = 0$ and always remains below $\eta^{(p)}$, even at $\gamma_0 = 0.7\tau^{-1}$. On the other hand, η_p for two-ring AFC starts at 0.9683 and becomes larger than $\eta^{(p)}$ just after $\gamma_0 = 0.0286\tau^{-1}$, where $\eta_p = \eta^{(p)} = 0.9676$. We note that the projection efficiency η_p decreases more slowly than the projected efficiency $\eta^{(p)}$ for both single-ring and two-ring AFC. But the initially larger value of 0.9683 for two-ring AFC allows η_p to overcome $\eta^{(p)}$ at just $\gamma_0 = 0.0286\tau^{-1}$.

Having computed the projected AFC efficiency $\eta^{(p)}$, it is interesting to compare it to its theoretical bounds, the
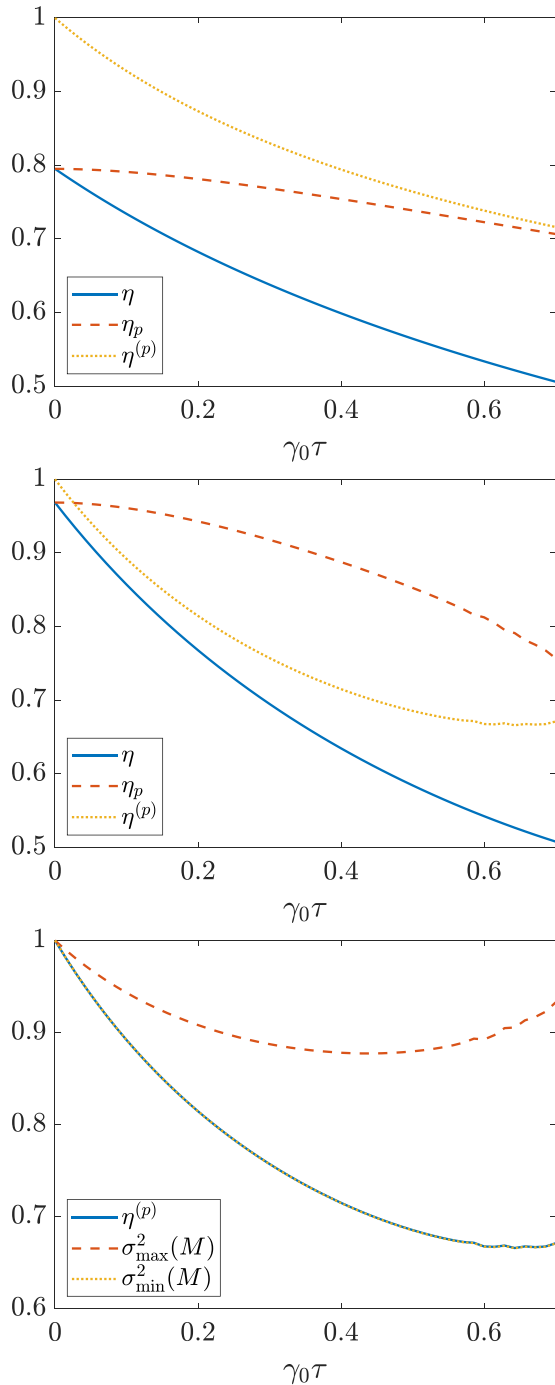
FIG. 10. Maximum overall efficiency η, and its corresponding projection efficiency η_p, and projected efficiency $\eta^{(p)}$ for single-ring AFC (top) and two-ring AFC (middle) as functions of γ_0. Comparison of the $\eta^{(p)}$ for a raised-cosine input, $\sigma^2_{\max}(M)$, and $\sigma^2_{\min}(M)$ as functions of γ_0 (bottom).

squared singular values of M. This is what we do in the last plot of Fig. 10, where $\eta^{(p)}$, $\sigma^2_{\max}(M)$ and $\sigma^2_{\min}(M)$ for optimal two-ring AFC are plotted as functions of $\gamma_0 \tau$ in a common axis. Indeed, we verify that $\eta^{(p)}$ lies within its theoretical bounds of $\sigma^2_{\min}(M)$ and $\sigma^2_{\max}(M)$. Moreover, $\eta^{(p)}$ follows closely $\sigma^2_{\max}(M)$. From Eq. (43), this implies that the projected input $|s^{(p)}_{\text{in}}(t)\rangle$ closely matches the right sin-

gular vector corresponding to $\sigma_{\min}(M)$. From Fig. 9, the rings' parameters are such that γ_0/γ_e is small compared to unity. From Fig. 7 we recall that the right singular vector corresponding to $\sigma_{\min}(M)$ for small γ_0/γ_e has Bloch components $-S^{(r)}_1(M) \approx 0$, $-S^{(r)}_2(M) \approx 0$, and $-S^{(r)}_3(M) \approx -1$. Recall that $S^{(r)}_j(M)$ were defined as the Bloch components of the right singular vector corresponding to $\sigma_{\max}(M)$, not $\sigma_{\min}(M)$. Thus, the right singular vector for $\sigma_{\min}(M)$ is approximately proportional to $|n^{(\text{in})}_2\rangle$. Hence, it is approximately proportional to $|u^*_{21}(t_m - t, 0)\rangle$, as follows from our basis definition in Eq. (38). Therefore, the close match between this right singular vector and $|s^{(p)}_{\text{in}}(t)\rangle$ agrees with our previous discussion of Fig. 8, where we observed that the raised-cosine input closely matches the time-reversed impulse response $u^*_{21}(t_m - t, 0)$.

Thus, we find that the AFC efficiency of the raised-cosine input is mostly determined by its close match to $u^*_{21}(t_m - t, 0)$ for $\gamma_e \gtrsim |\kappa_e|$, and $\gamma_e \gg \gamma_0$. This implies that any input pulse shape that matches closely $u^*_{21}(t_m - t, 0)$ under these conditions also achieves similar optimal AFC efficiencies. From Fig. 2 we recall that $u_{21}(t, 0)$ for $\gamma_e \gtrsim |\kappa_e|$, and $\gamma_e \gg \gamma_0$ has an envelope continuous at $t = 0$, most of its energy in its first lobe, and small-amplitude oscillations (if underdamped) at its tail for $\gamma_e t \gtrsim 1$. Hence, symmetric, single-lobe pulses in general (e.g., Gaussian, super-Gaussian, and hyperbolic secant), rather than just the raised-cosine pulse in particular, closely match the time-reversed impulse response $u^*_{21}(t_m - t, 0)$ and therefore may attain similar high AFC efficiencies under analogous conditions.

IX. CONCLUSION

The efficiency of adiabatic frequency conversion (AFC) for a single-ring resonator is known to be limited to below 80% for input pulses with a symmetric single peak. This is a consequence of a relatively poor match between the pulse's shape and the ring's impulse response. To overcome this limitation, we propose inducing AFC simultaneously over two coupled rings, rather than a single one.

We analyze the efficiency of AFC in this two-ring system using temporal coupled mode theory. In this manner we show that the AFC efficiency for symmetric, single-lobe pulses in two-ring devices has an upper limit of 97% when intrinsic ring losses are comparatively small; interring coupling is slightly underdamped; extrinsic decay is comparable to the input bandwidth; and ring modulation occurs slightly after the input pulse's maximum. To explain this higher AFC efficiency, we analyze the AFC process as a linear operator in the vector space of finite-energy pulses. More specifically, we examine the AFC process as a composition of two linear maps: one representing loading of the input pulse's energy into the rings and another describing unloading of the rings's energy into a frequency-shifted output pulse. We use orthonormal representation theory to represent these maps as 2×2 matrices. This allows us examine each matrix's singular value decomposition, which we demonstrate to govern the AFC process's efficiency.

We expect that our results will stimulate experimental work on our proposed two-ring configuration. Moreover, the matrix analysis developed in this work can be extended to

analyze more complicated, multiring networks for tunable frequency conversion with high efficiency on integrated photonic chips.

APPENDIX A: CHARACTERIZATION OF THE IMPULSE-RESPONSE FUNCTIONS

In this Appendix we examine analytically the impulse-response functions $u_{nm}(t, \Delta)$, defined by Eq. (17). Our objective is to describe their properties, which are useful for our study of AFC. For succinctness, we first factorize these functions as

$$u_{nm}(t, \Delta) = \tilde{u}_{nm}(t) \exp\left[-i(\omega_0 + \Delta)t - \bar{\gamma}t\right]\Theta(t). \quad (A1)$$

Here, as in Eq. (6), ω_0 is the rings' original resonance frequency; $\Theta(t)$, the Heaviside step function; and $\bar{\gamma}$ the average ring decay rate

$$\bar{\gamma} = (\gamma_1 + \gamma_2)/2. \quad (A2)$$

The expressions for the factorized functions $\bar{u}_{nm}(t)$ provided below can be obtained by solving the TCMT equations, Eq. (1), for constant $H(t)$ using the Laplace-transform method.

Similarly to a damped harmonic oscillator [52,53], the interring coupling (and thus, the impulse-response functions) can be underdamped, critically damped, or overdamped. Interring coupling is underdamped when

$$|\kappa| > \gamma_e/2. \quad (A3)$$

In this case the impulse-response functions exhibit oscillatory behavior and their expressions are given by

$$\tilde{u}_{11}(t) = \cos(\Omega t/2) - (\gamma_e/\Omega)\sin(\Omega t/2),$$

$$\tilde{u}_{12}(t) = (2i\kappa/\Omega)\sin(\Omega t/2),$$

$$\tilde{u}_{21}(t) = (2i\kappa^*/\Omega)\sin(\Omega t/2),$$

$$\tilde{u}_{22}(t) = \cos(\Omega t/2) + (\gamma_e/\Omega)\sin(\Omega t/2). \quad (A4)$$

Here Ω is the frequency of energy exchange, analogous to the Rabi frequency in a quantum-mechanical two-level system. It is given by

$$\Omega = \sqrt{4|\kappa|^2 - \gamma_e^2}. \quad (A5)$$

Interring coupling is critically damped when

$$|\kappa| = \gamma_e/2. \quad (A6)$$

In this case, the factor functions $\tilde{u}_{nm}(t)$ in Eq. (A1) become affine functions of time, specifically

$$\tilde{u}_{11}(t) = 1 - \gamma_e t/2,$$

$$\tilde{u}_{12}(t) = i\kappa t,$$

$$\tilde{u}_{21}(t) = i\kappa^* t,$$

$$\tilde{u}_{22}(t) = 1 + \gamma_e t/2. \quad (A7)$$

Interring coupling is overdamped when

$$|\kappa| < \gamma_e/2. \quad (A8)$$

In this case the factor functions $\tilde{u}_{nm}(t)$ become sums of hyperbolic functions of time; explicitly

$$\tilde{u}_{11}(t) = \cosh(\xi t/2) - (\gamma_e/\xi)\sinh(\xi t/2),$$

$$\tilde{u}_{12}(t) = (2i\kappa/\xi)\sinh(\xi t/2),$$

$$\tilde{u}_{21}(t) = (2i\kappa^*/\xi)\sinh(\xi t/2),$$

$$\tilde{u}_{22}(t) = \cosh(\xi t/2) + (\gamma_e/\xi)\sinh(\xi t/2). \quad (A9)$$

Here ξ is the positive rate

$$\xi = \sqrt{\gamma_e^2 - 4|\kappa|^2}. \quad (A10)$$

Regardless of the damping regime, the column vector $(u_{11}(t, \Delta), u_{21}(t, \Delta))^T$ $[(u_{12}(t, \Delta), u_{22}(t, \Delta))^T]$ is a solution of the TCMT equation, i.e., Eq. (1), with $H(t) = H_m$, $s_+(t) = 0$ and initial condition $a(0) = (1, 0)^T$ $[a(0) = (0, 1)^T]$. Consequently, they have the initial values

$$u_{11}(0) = 1, \quad u_{12}(0) = 0,$$

$$u_{21}(0) = 0, \quad u_{22}(0) = 1. \quad (A11)$$

Additionally, the envelope functions $\bar{u}_{nm}(t) = u_{nm}(t, \Delta)\exp[i(\omega_0 + \Delta)t]$ have the initial values for their time derivatives given by

$$\frac{d\bar{u}_{11}(0)}{dt} = -\gamma_1, \quad \frac{d\bar{u}_{12}(0)}{dt} = i\kappa,$$

$$\frac{d\bar{u}_{21}(0)}{dt} = i\kappa^*, \quad \frac{d\bar{u}_{22}(0)}{dt} = -\gamma_2. \quad (A12)$$

Although the expressions in Eqs. (A4), (A7), and (A9) appear qualitatively different, they are continuous functions of the ring parameters (i.e., κ, γ_e, and γ_0), even at the parameter transition between underdamped and overdamped coupling [i.e., in the neighborhood of Eq. (A6)].

The behavior of the impulse-response functions $u_{nm}(t, \Delta)$ in the underdamped and critically damped regimes is straightforward to interpret. However, their behavior in the overdamped regime merits some discussion. Only the impulse-response functions $u_{11}(t, \Delta)$, $u_{12}(t, \Delta)$, and $u_{21}(t, \Delta)$ are relevant for our investigation of AFC. Furthermore, $u_{12}(t, \Delta)$ and $u_{12}(t, \Delta)$ are always proportional, so we analyze only $u_{11}(t, \Delta)$ and $u_{21}(t, \Delta)$. First, we consider the forms of these functions for large, positive values of t. Specifically, for $t \gg 2\xi^{-1}$, we may approximate the hyperbolic functions in Eq. (A9) as $\sinh(x) \approx \cosh(x) \approx \exp(x)/2$. Then, to the accuracy of this approximation, the factor functions $\tilde{u}_{11}(t)$ and $\tilde{u}_{21}(t)$ become

$$\tilde{u}_{11}(t) \approx \tfrac{1}{2}(1 - \gamma_e/\xi)\exp(\xi t/2),$$

$$\tilde{u}_{21}(t) \approx (i\kappa^*/\xi)\exp(\xi t/2). \quad (A13)$$

Consequently, for $t \gg 2\xi^{-1}$, $u_{11}(t)$ and $u_{21}(t)$ decay in magnitude as $\exp[-(\bar{\gamma} - \xi/2)t]$. Moreover, we find that for large t, $\bar{u}_{11}$ is always negative. This follows because the factor $(1 - \gamma_e/\xi)$ itself is negative as a consequence of the assumed overdamping condition, Eq. (A8), and of the definition of ξ in Eq. (A10).

We also point out that, in the overdamped regime, the envelopes $\bar{u}_{11}(t) = u_{11}(t, \Delta)\exp[i(\omega_0 + \Delta)t]$ and $\bar{u}_{21}(t) = u_{21}(t, \Delta)\exp[i(\omega_0 + \Delta)t]$ always have a single extremum each. In other words, for each envelope there exists one and

only one positive time t such that $\frac{d\bar{u}_{1n}}{dt} = 0$ ($n = 1, 2$). We first prove this statement for $\bar{u}_{11}(t)$. By differentiation of Eq. (A9), the condition $\frac{d\bar{u}_{11}}{dt} = 0$ in the overdamped regime is equivalent to

$$\tanh(\xi t/2) = \frac{\bar{\gamma} + \gamma_e/2}{\gamma_e \bar{\gamma}/\xi + \xi/2}. \qquad (A14)$$

The left-hand side of Eq. (A14) is a monotonically increasing function of t, while its right-hand side is time-independent constant. Thus, there is, at most, one value of t for which the left-hand side of Eq. (A14) equals its right-hand side. But $\frac{d\bar{u}_{11}}{dt}$ is negative when $t = 0$ and it converges to a positive value for $t \to \infty$, as can be seen from Eq. (A13). So there must be at least one positive value of t for which $\frac{d\bar{u}_{11}}{dt} = 0$. Hence, there exists exactly one positive value of t for which $\frac{d\bar{u}_{11}}{dt}$ vanishes. By an analogous argument, we can prove that there is exactly one positive value of t for which $\frac{d\bar{u}_{21}}{dt}$ vanishes.

Next, we evaluate the inner products required for our AFC efficiency analysis in terms of the ring parameters. Given Eqs. (A4), (A7), and (A9) for the factor functions $\bar{u}_{nm}(t)$, we next subsitute them back into Eq. (A1) and into the inner-product definition in Eq. (11). Then, employing elementary integration techniques, we obtain

$$\langle u_{11}|u_{11}\rangle = \frac{\gamma_2(\gamma_1 + \gamma_2) + |\kappa|^2}{2(\gamma_1 + \gamma_2)(\gamma_1\gamma_2 + |\kappa|^2)},$$

$$\langle u_{11}|u_{12}\rangle = \frac{i\kappa\gamma_2}{2(\gamma_1 + \gamma_2)(\gamma_1\gamma_2 + |\kappa|^2)},$$

$$\langle u_{12}|u_{12}\rangle = \frac{|\kappa|^2}{2(\gamma_1 + \gamma_2)(\gamma_1\gamma_2 + |\kappa|^2)}. \qquad (A15)$$

As in the main text, $\langle u_{nm}|u_{pq}\rangle$ is an abbreviation for $\langle u_{nm}(t, \Delta)|u_{pq}(t, \Delta)\rangle$. We note that, for our investigation of AFC, we require only the inner products of impulse-response functions $u_{nm}(t, \Delta)$ with equal frequency shift Δ. Because of the aforementioned continuity of the impulse-response functions with respect to the ring parameters, Eq. (A15) holds regardless of whether the interring coupling is underdamped, critically damped, or overdamped.

As seen in Eqs. (A4), (A7), and (A9), $u_{21}(t, \Delta)$ is always proportional to $u_{12}(t, \Delta)$. Therefore, we may evaluate the inner products of $u_{21}(t, \Delta)$ with other functions from those of $u_{12}(t, \Delta)$. In this way, we have

$$\langle u_{11}|u_{21}\rangle = (\kappa^*/\kappa)\langle u_{11}|u_{12}\rangle,$$

$$\langle u_{21}|u_{21}\rangle = \langle u_{12}|u_{12}\rangle. \qquad (A16)$$

In Eq. (A16) we assume that $\kappa \neq 0$. Otherwise both $u_{12}(t, \Delta)$ and $u_{21}(t, \Delta)$ vanish, and so do their inner products with any function.

As a consequence of Eq. (A15), for nonzero interring coupling κ, $u_{11}(t, \Delta)$ and $u_{12}(t, \Delta)$ [and consequently $u_{11}(t, \Delta)$ and $u_{21}(t, \Delta)$] are mutually orthogonal if and only if $\gamma_2 = 0$. As a consequence of Eq. (4), $\gamma_2 = 0$ if and only if the intrinsic decay rate γ_0 vanishes. Furthermore, if $\gamma_0 = 0$, then Eq. (A15)

simplifies to

$$\langle u_{11}|u_{11}\rangle = \frac{1}{2\gamma_1},$$

$$\langle u_{11}|u_{12}\rangle = 0,$$

$$\langle u_{12}|u_{12}\rangle = \frac{1}{2\gamma_1}. \qquad (A17)$$

In Secs. V and VI, we find it useful to introduce the effective cosine $\cos\theta_{12}$ in Eq. (48) as a normalized measure of the collinearity between $u_{11}(t, \Delta)$ and $u_{21}(t, \Delta)$. Here we provide an explicit expression for it in terms of the ring parameters, we bound its value, and we investigate it in the limit of large intrinsic loss.

To obtain the expression for $\cos\theta_{12}$ in terms of the rings' TCMT parameters, we directly substitute the expressions for the inner products in Eq. (A15) and (A16) into the definition of Eq. (48). In this way we get

$$\cos^2\theta_{12} = \frac{\gamma_2^2}{\gamma_2(\gamma_1 + \gamma_2) + |\kappa|^2}. \qquad (A18)$$

As expected, $\cos\theta_{12} \in [0, 1]$. Furthermore, it increases monotonically with γ_2 for fixed γ_1 and $|\kappa|$, and with γ_0 for fixed γ_e and $|\kappa|$, though it decreases with $|\kappa|$ for fixed γ_1 and γ_2, or equivalently, fixed γ_0 and γ_e. This agrees with the behavior observed in Fig. 3.

Next, we utilize Eq. (A18) to obtain an upper bound for $\cos\theta_{12}$ tighter than $\cos\theta_{12} \leqslant 1$, which follows from the Schwarz inequality. To do so, we first note that $\cos\theta_{12}$ is maximized with respect to $|\kappa|$ when $|\kappa| = 0$. Likewise, we note that $\cos\theta_{12}$ for $|\kappa| = 0$ is largest when $\gamma_e = 0$. In this way we obtain

$$\cos^2\theta_{12} \leqslant \frac{\gamma_2}{\gamma_1 + \gamma_2} = \frac{\gamma_0}{2\gamma_0 + \gamma_e} \leqslant \frac{1}{2}. \qquad (A19)$$

Hence, we find that $\cos\theta_{12} \leqslant 1/\sqrt{2}$. Then, because Eq. (A19) prohibits $\cos\theta_{12} = 1$, we conclude from the Schwarz inequality that $u_{11}(t, \Delta)$ and $u_{21}(t, \Delta)$ are never collinear, as then $\cos\theta_{12}$ would equal unity. This result is relevant because it implies that the AFC operator $\hat{T}$ in a two-ring system always is of rank two.

Lastly, we note that it follows from Eq. (A18) that

$$\lim_{\gamma_0 \to \infty} \cos\theta_{12} = 1/\sqrt{2}, \qquad (A20)$$

assuming that, in this limit, γ_e and $|\kappa|$ remain finite. Combining Eqs. (A19) and (A20), we further conclude that $\cos\theta_{12}$ converges to $1/\sqrt{2}$ always from below in the limit $\gamma_0 \to \infty$.

APPENDIX B: GRAM-SCHMIDT ORTHONORMALIZATION OF AFC IMAGE AND COIMAGE

In this Appendix we use the Gram-Schmidt process [45,46] to obtain orthonormal bases for both the image $\mathcal{V}_{\text{out}}$ and the coimage $\mathcal{V}_{\text{in}}$ of the AFC operator $\hat{T}$. Then we use them to derive results useful to the main text. First, we find explicit expressions for the matrices M_{in} and M_{out} representing the maps $\hat{T}_{\text{in}}$ and $\hat{T}_{\text{out}}$ in these bases. Then we obtain formulas

for the projected input $|s_{\text{in}}^{(p)}(t)\rangle$ and its energy in terms of the ring amplitudes at the time of modulation and of the rings' parameters.

We first write expressions for the basis vectors $|n_1^{(\text{in})}\rangle$ and $|n_2^{(\text{in})}\rangle$ spanning $\mathcal{V}_{\text{in}}$. We recall from Sec. IV that these are defined to satisfy the conditions in Eq. (38). These conditions uniquely determine $|n_1^{(\text{in})}\rangle$ and $|n_2^{(\text{in})}\rangle$ as

$$|n_2^{(\text{in})}\rangle = \frac{|u_{21}^*(t_m - t, 0)\rangle}{\sqrt{\langle u_{21}|u_{21}\rangle}},$$

$$|n_1^{(\text{in})}\rangle = \frac{|N_1^{(\text{in})}\rangle}{\sqrt{\langle N_1^{(\text{in})}|N_1^{(\text{in})}\rangle}}, \quad \text{(B1)}$$

where the auxiliary vector $|N^{(\text{in})}\rangle$ is defined as

$$|N_1^{(\text{in})}\rangle = |u_{11}^*(t_m - t, 0)\rangle$$
$$- |u_{21}^*(t_m - t, 0)\rangle \frac{\langle u_{11}|u_{21}\rangle}{\langle u_{21}|u_{21}\rangle}. \quad \text{(B2)}$$

From Eq. (B2) it follows that the squared norm of $|N_1^{(\text{in})}\rangle$ is given by

$$\langle N_1^{(\text{in})}|N_1^{(\text{in})}\rangle = \langle u_{11}|u_{11}\rangle - \frac{|\langle u_{11}|u_{21}\rangle|^2}{\langle u_{21}|u_{21}\rangle}. \quad \text{(B3)}$$

The inner products in Eqs. (B1) to (B3) can be evaluated in terms of the rings' TCMT parameters using Eqs. (A15) and (A16).

Note that in writing Eqs. (B1) to (B3), we repeatedly use the fact that

$$\langle f(t_m - t)|g(t_m - t)\rangle = \langle f(t)|g(t)\rangle \quad \text{(B4)}$$

for any real value of t_m, as follows from the inner product definition, Eq. (11).

In an analogous way, we define the orthonormal basis vectors $|n_1^{(\text{out})}\rangle$ and $|n_2^{(\text{out})}\rangle$ spanning the image $\mathcal{V}_{\text{out}}$ of $\hat{T}$. These are then given by

$$|n_2^{(\text{out})}\rangle = \frac{|u_{12}(t - t_m, \Delta)\rangle}{\sqrt{\langle u_{12}|u_{12}\rangle}},$$

$$|n_1^{(\text{out})}\rangle = \frac{|N_1^{(\text{out})}\rangle}{\sqrt{\langle N_1^{(\text{out})}|N_1^{(\text{out})}\rangle}}, \quad \text{(B5)}$$

with

$$|N_1^{(\text{out})}\rangle = |u_{11}(t - t_m, \Delta)\rangle$$
$$- |u_{12}(t - t_m, \Delta)\rangle \frac{\langle u_{12}|u_{11}\rangle}{\langle u_{12}|u_{12}\rangle} \quad \text{(B6)}$$

and

$$\langle N_1^{(\text{out})}|N_1^{(\text{out})}\rangle = \langle u_{11}|u_{11}\rangle - \frac{|\langle u_{11}|u_{12}\rangle|^2}{\langle u_{12}|u_{12}\rangle}. \quad \text{(B7)}$$

The inner products in Eqs. (B5) to (B7) can be evaluated in terms of the rings' TCMT parameters using Eq. (A15).

With the explicit expressions for the orthonormal bases $\{|n_1^{(\text{in})}\rangle, |n_2^{(\text{in})}\rangle\}$ and $\{|n_1^{(\text{out})}\rangle, |n_2^{(\text{out})}\rangle\}$ in Eqs. (B1) and (B5), we may write corresponding expressions for the loading matrix M_{in} and the unloading matrix M_{out}. Substituting then

Eqs. (B1) and (B5) into Eq. (40), we obtain

$$M_{\text{in}} = \sqrt{2\gamma_e} \begin{pmatrix} \sqrt{\langle N_1^{(\text{in})}|N_1^{(\text{in})}\rangle} & \langle u_{21}|u_{11}\rangle/\sqrt{\langle u_{21}|u_{21}\rangle} \\ 0 & \sqrt{\langle u_{21}|u_{21}\rangle} \end{pmatrix},$$

$$M_{\text{out}} = \sqrt{2\gamma_e} \begin{pmatrix} \sqrt{\langle N_1^{(\text{out})}|N_1^{(\text{out})}\rangle} & 0 \\ \langle u_{12}|u_{11}\rangle/\sqrt{\langle u_{12}|u_{12}\rangle} & \sqrt{\langle u_{12}|u_{12}\rangle} \end{pmatrix}. \quad \text{(B8)}$$

Next, we derive expressions for thr projected input $|s_{\text{in}}^{(p)}(t)\rangle$ and its energy, $\langle s_{\text{in}}^{(p)}(t)|s_{\text{in}}^{(p)}(t)\rangle$ in terms of the rings' amplitude vector $a(t_m)$ at the time of modulation. To achieve this, we write the projector $\hat{P}_{\text{in}}$, introduced in Sec. III, as [47]

$$\hat{P}_{\text{in}} = \sum_{j=1}^{2} |n_j^{(\text{in})}\rangle\langle .| \quad \text{(B9)}$$

Thus, we may write the projected input as

$$|s_{\text{in}}^{(p)}(t)\rangle = \sum_{j=1}^{2} |n_j^{(\text{in})}\rangle\langle n_j^{(\text{in})}|s_{\text{in}}(t)\rangle, \quad \text{(B10)}$$

and its energy as

$$\langle s_{\text{in}}^{(p)}(t)|s_{\text{in}}^{(p)}(t)\rangle = \sum_{j=1}^{2} |\langle n_j^{(\text{in})}|s_{\text{in}}(t)\rangle|^2. \quad \text{(B11)}$$

Given Eq. (B1) for $|n_1^{(\text{in})}\rangle$ and $|n_2^{(\text{in})}\rangle$, we need only expressions for the inner products $\langle n_1^{(\text{in})}|s_{\text{in}}(t)\rangle$ and $\langle n_2^{(\text{in})}|s_{\text{in}}(t)\rangle$ to evaluate Eqs. (B10) and (B11). To do so, we recall from Eq. (18) that the ring amplitudes $a_j(t_m)$ may be written as

$$a_j(t_m) = \sqrt{2\gamma_e}\langle u_{j1}^*|s_{\text{in}}(t)\rangle \quad \text{(B12)}$$

for $j = 1, 2$. Then we utilize the adjoint of Eq. (B1) and Eq. (B12) to obtain

$$\langle n_2^{(\text{in})}|s_{\text{in}}(t)\rangle = \frac{a_2(t_m)}{\sqrt{2\gamma_e\langle u_{21}|u_{21}\rangle}},$$

$$\langle n_1^{(\text{in})}|s_{\text{in}}(t)\rangle = \frac{\langle N_1^{(\text{in})}|s_{\text{in}}(t)\rangle}{\sqrt{\langle N_1^{(\text{in})}|N_1^{(\text{in})}\rangle}}, \quad \text{(B13)}$$

where $\langle N_1^{(\text{in})}|s_{\text{in}}(t)\rangle$ is evaluated through

$$\langle N_1^{(\text{in})}|s_{\text{in}}(t)\rangle = \frac{a_1(t_m)}{\sqrt{2\gamma_e}} - \frac{a_2(t_m)\langle u_{21}|u_{11}\rangle}{\sqrt{2\gamma_e}\langle u_{21}|u_{21}\rangle}. \quad \text{(B14)}$$

APPENDIX C: PARTIAL ANALYTICAL SVD OF THE LOADING AND UNLOADING MATRICES

In this Appendix we investigate analytically the SVD of the loading and unloading matrices, M_{in} and M_{out}. To do so, let us first define the auxiliary matrices

$$K_{\text{in}} \equiv \hat{T}_{\text{in}}\hat{T}_{\text{in}}^{\dagger} = M_{\text{in}}M_{\text{in}}^{\dagger},$$
$$= 2\gamma_e \begin{pmatrix} \langle u_{11}|u_{11}\rangle & \langle u_{21}|u_{11}\rangle \\ \langle u_{11}|u_{21}\rangle & \langle u_{21}|u_{21}\rangle \end{pmatrix} \quad \text{(C1)}$$

and

$$K_{\text{out}} \equiv \hat{T}_{\text{out}}^{\dagger} \hat{T}_{\text{out}} = M_{\text{out}}^{\dagger} M_{\text{out}},$$

$$= 2\gamma_e \begin{pmatrix} \langle u_{11}|u_{11}\rangle & \langle u_{11}|u_{12}\rangle \\ \langle u_{12}|u_{11}\rangle & \langle u_{12}|u_{12}\rangle \end{pmatrix} \quad \text{(C2)}$$

By construction, the eigenvalues of K_{in} are the squared singular values of M_{in}, and its eigenvectors are the left singular vectors of M_{in} [50,51]. Similarly, the eigenvalues of K_{out} are the squared singular values of M_{out}, and its eigenvectors are the right singular vectors of M_{out}.

Then, by finding the eigenvalues of K_{in}, we verify that the squared singular values of M_{in} are indeed given by Eq. (52). Moreover, finding the eigenvalues of K_{out} and recalling Eq. (A16), we find that K_{in} and K_{out} have the same eigenvalues. Therefore, M_{in} and M_{out} have the same singular values, as stated in Eq. (51).

Next, we determine the Bloch components $S_j^{(l)}(M_{\text{in}})$ and $S_j^{(r)}(M_{\text{out}})$ of the left singular vector of M_{in} with largest singular value and of the right sisngular vector of M_{out} with largest singular value. To do this we obtain the components of K_{in} and K_{out} in the basis of the Pauli matrices. Let $k_{\text{in}}^{(j)}$ be the components of K_{in} and $k_{\text{out}}^{(j)}$ be those of K_{out} ($j = 1, 2, 3$). These are computed through the formula [60,62]

$$k_{\text{in}}^{(j)} = \tfrac{1}{2}\text{Tr}\{K_{\text{in}}s_j\}, \quad k_{\text{out}}^{(j)} = \tfrac{1}{2}\text{Tr}\{K_{\text{out}}s_j\}. \quad \text{(C3)}$$

Here $\text{Tr}\{A\}$ is the trace of A, and s_j are the Pauli matrices, as in Eq. (55). Thus, we substitute Eqs. (C1) and (C2) into Eq. (C3) to find $k_{\text{in}}^{(j)}$ and $k_{\text{out}}^{(j)}$ in terms of the impulse-response inner

products. Then we substitute Eqs. (A15) and (A16) to find them in terms of the ring parameters. In this way we obtain

$$k_{\text{in}}^{(1)} = 2\gamma_e \text{Re}\{\langle u_{11}|u_{21}\rangle\} = \mu_k \text{Im}\{\kappa\},$$

$$k_{\text{in}}^{(2)} = 2\gamma_e \text{Im}\{\langle u_{11}|u_{21}\rangle\} = \mu_k \text{Re}\{\kappa\},$$

$$k_{\text{in}}^{(3)} = \gamma_e(\langle u_{11}|u_{11}\rangle - \langle u_{21}|u_{21}\rangle) = \mu_k \bar{\gamma}, \quad \text{(C4)}$$

and

$$k_{\text{out}}^{(1)} = 2\gamma_e \text{Re}\{\langle u_{12}|u_{11}\rangle\} = -\mu_k \text{Im}\{\kappa\},$$

$$k_{\text{out}}^{(2)} = 2\gamma_e \text{Im}\{\langle u_{12}|u_{11}\rangle\} = -\mu_k \text{Re}\{\kappa\},$$

$$k_{\text{out}}^{(3)} = \gamma_e(\langle u_{11}|u_{11}\rangle - \langle u_{12}|u_{12}\rangle) = \mu_k \bar{\gamma}. \quad \text{(C5)}$$

where the factor μ_k is given by

$$\mu_k = \frac{\gamma_2 \gamma_e}{(\gamma_1 + \gamma_2)(\gamma_1\gamma_2 + |\kappa|^2)}. \quad \text{(C6)}$$

Given Eqs. (C4) and (C5), we may now evaluate the Bloch components $S_j^{(l)}(M_{\text{in}})$ and $S_j^{(r)}(M_{\text{out}})$, as intended. To do so, we need only one result from spinor theory. This is that the Bloch components (i.e., the normalized Stokes parameters) of the eigenvectors of K_{in} and K_{out} with largest eigenvalue equal $k_{\text{in}}^{(j)}$ and $k_{\text{out}}^{(j)}$ after these are normalized so their squares add up to unity [62]. With this result, along with Eqs. (C4) and (C5), we confirm that $S_j^{(l)}(M_{\text{in}})$ and $S_j^{(r)}(M_{\text{out}})$ are given by Eqs. (56) and (57).

Lastly, we prove Eq. (60) relating the Bloch components $S_j^{(r)}(M_{\text{in}})$ and $S_j^{(l)}(M_{\text{out}})$. To do this, we evaluate the matrix products

$$M_{\text{in}}^{\dagger} M_{\text{in}} = 2\gamma_e \begin{pmatrix} \langle N_1^{(\text{in})}|N_1^{(\text{in})}\rangle & \langle u_{21}|u_{11}\rangle\sqrt{\langle N_1^{(\text{in})}|N_1^{(\text{in})}\rangle/\langle u_{21}|u_{21}\rangle} \\ \langle u_{11}|u_{21}\rangle\sqrt{\langle N_1^{(\text{in})}|N_1^{(\text{in})}\rangle/\langle u_{21}|u_{21}\rangle} & \langle u_{21}|u_{21}\rangle + |\langle u_{11}|u_{21}\rangle|^2/\langle u_{21}|u_{21}\rangle \end{pmatrix},$$

$$M_{\text{out}} M_{\text{out}}^{\dagger} = 2\gamma_e \begin{pmatrix} \langle N_1^{(\text{out})}|N_1^{(\text{out})}\rangle & \langle u_{11}|u_{12}\rangle\sqrt{\langle N_1^{(\text{out})}|N_1^{(\text{out})}\rangle/\langle u_{12}|u_{12}\rangle} \\ \langle u_{12}|u_{11}\rangle\sqrt{\langle N_1^{(\text{in})}|N_1^{(\text{in})}\rangle/\langle u_{21}|u_{21}\rangle} & \langle u_{12}|u_{12}\rangle + |\langle u_{11}|u_{12}\rangle|^2/\langle u_{12}|u_{12}\rangle \end{pmatrix}. \quad \text{(C7)}$$

We note that the right singular vectors of M_{in} are the eigenvectors of $M_{\text{in}}^{\dagger} M_{\text{in}}$, and the left singular vectors of M_{out} are the eigenvectors of $M_{\text{out}} M_{\text{out}}^{\dagger}$. Hence, the Bloch components $S_j^{(r)}(M_{\text{in}})$ and $S_j^{(l)}(M_{\text{out}})$ can be evaluated from Eq. (C7), just as $S_j^{(l)}(M_{\text{in}})$ and $S_j^{(r)}(M_{\text{out}})$ were obtained from Eqs. (C1) and (C2) for K_{in} and K_{out}.

However, rather than obtaining explicit expressions for $S_j^{(r)}(M_{\text{in}})$ and $S_j^{(l)}(M_{\text{out}})$ and comparing them, we need only make two observations about the entries of $M_{\text{in}}^{\dagger} M_{\text{in}}$ and $M_{\text{out}} M_{\text{out}}^{\dagger}$ in Eq. (C7) to establish the desired results, Eq. (60). First, we note that the value of these diagonal entries of $M_{\text{in}}^{\dagger} M_{\text{in}}$ and $M_{\text{out}} M_{\text{out}}^{\dagger}$ are identical, as a consequence of Eq. (A16). Hence, we get $S_3^{(r)}(M_{\text{in}}) = S_3^{(l)}(M_{\text{out}})$. Second, the ratio between the first-row off-diagonal element of $M_{\text{in}}^{\dagger} M_{\text{in}}$ and that of $M_{\text{out}} M_{\text{out}}^{\dagger}$ equals $\langle u_{21}|u_{11}\rangle/\langle u_{11}|u_{12}\rangle$, again recalling Eq. (A16). This is the same case as for K_{in} and K_{out}.

Therefore, we obtain $S_1^{(r)}(M_{\text{in}}) = -S_1^{(l)}(M_{\text{out}})$ and $S_2^{(r)}(M_{\text{in}}) = -S_2^{(l)}(M_{\text{out}})$, just as in Eq. (58).

APPENDIX D: PROOF OF SUBMULTIPLICATIVE PROPERTY OF MAXIMUM AND MINIMUM SINGULAR VALUES

In Sec. VII we are interested in relating the minimum and maximum singular values of a matrix product to those of its factors. Let $\sigma_{\text{max}}(M)$ [$\sigma_{\text{min}}(M)$] be the maximum (minimum) singular value of some matrix M. In this Appendix we prove that, for any matrices A and B for which their product AB exists, $\sigma_{\text{max}}(AB)$ [$\sigma_{\text{min}}(AB)$] is bounded above (below) by

$$\sigma_{\text{max}}(AB) \leqslant \sigma_{\text{max}}(A)\sigma_{\text{max}}(B), \quad \text{(D1)}$$

$$\sigma_{\text{min}}(AB) \geqslant \sigma_{\text{min}}(A)\sigma_{\text{min}}(B). \quad \text{(D2)}$$

In the context of matrix norms (or operator norms), the maximum singular value is proven to be a matrix norm [50], and Eq. (D1) is referred to as its submultiplicative property.

A similar proof of Eq. (D1) for bounded operators in a Hilbert space is given in Ref. [45], Ch. 17. Though our proof is more detailed, including discussion of sufficient conditions for Eq. (D1) to be an equality. Of course, we have also extended the proof of Eq. (D1) to also prove Eq. (D2).

We start with the proof of Eq. (D1). From Refs. [49,50], $\sigma_{\max}(M)$ can be written as

$$\sigma_{\max}^2(M) = \max_{x \neq 0} \frac{x^\dagger M^\dagger M x}{x^\dagger x} \tag{D3}$$

In other words, $\sigma_{\max}^2(M)$ is the maximum value of the quotient in the right-hand side of Eq. (D3). As mentioned in Sec. IV, the right-hand side of Eq. (D3) is a Rayleigh quotient.

Momentarily, we assume that the vector x which maximizes the right-hand side of Eq. (D3) for $M = AB$ is such that $Bx \neq 0$, and consequently $x^\dagger B^\dagger Bx = \|Bx\|^2 > 0$. Then we may write

$$\begin{aligned} \sigma_{\max}^2(AB) &= \max_{x \neq 0} \frac{x^\dagger B^\dagger A^\dagger ABx}{x^\dagger B^\dagger Bx} \frac{x^\dagger B^\dagger Bx}{x^\dagger x}, \\ &\leqslant \max_{x \neq 0} \frac{x^\dagger B^\dagger A^\dagger ABx}{x^\dagger B^\dagger Bx} \max_{x \neq 0} \frac{x^\dagger B^\dagger Bx}{x^\dagger x}, \\ &= \max_{x \neq 0} \frac{x^\dagger B^\dagger A^\dagger ABx}{x^\dagger B^\dagger Bx} \sigma_{\max}^2(B). \end{aligned} \tag{D4}$$

In Eq. (D4) we made use of Eq. (D3) for $M = B$.

Next, we bound from above the first factor in the last line of Eq. (D4). Thus, we write

$$\max_{x \neq 0} \frac{x^\dagger B^\dagger A^\dagger ABx}{x^\dagger B^\dagger Bx} \leqslant \max_{y \neq 0} \frac{y^\dagger A^\dagger Ay}{y^\dagger y} = \sigma_{\max}^2(A). \tag{D5}$$

The inequality in Eq. (D5) becomes an equality if and only if a right singular vector of A with its largest singular value is in the range of B. Of course, this is the case if B is a square matrix of full rank. Finally, substituting Eq. (D5) into (D4), we obtain the desired bound, Eq. (D1).

Now, if the vector x maximizing the right-hand side of Eq. (D3) for $M = AB$ is such that $Bx = 0$, then $\sigma_{\max}(AB) = 0$. Then Eq. (D1) is trivially satisfied, as the singular values are non-negative by definition.

Next, we show that if the left singular vector of B corresponding to $\sigma_{\max}(B)$ equals the right singular vector of A corresponding to $\sigma_{\max}(A)$, then Eq. (D1) is an equality. In this case, let x be the right singular vector of B corresponding to

$\sigma_{\max}(B)$. Then

$$\begin{aligned} \sigma_{\max}^2(A)\sigma_{\max}^2(B) &= \frac{x^\dagger B^\dagger A^\dagger ABx}{x^\dagger B^\dagger Bx} \frac{x^\dagger B^\dagger Bx}{x^\dagger x} \\ &= \frac{x^\dagger B^\dagger A^\dagger ABx}{x^\dagger x} \\ &\leqslant \sigma_{\max}^2(AB). \end{aligned} \tag{D6}$$

Here we used Eq. (D3) with $M = AB$. But for Eq. (D6) to be compatible with the Eq. (D1), the inequality in the last line of Eq. (D6) must be an equality. This completes the proof.

Now, we prove Eq. (D2). Similarly to Eq. (D3), the minimum singulvar value $\sigma_{\min}(M)$ of some matrix M satisfies the relation [49],

$$\sigma_{\min}^2(M) = \min_{x \neq 0} \frac{x^\dagger M^\dagger M x}{x^\dagger x}. \tag{D7}$$

Momentarily, we assume that $Bx = 0$ if and only if $x = 0$ Then, $x^\dagger B^\dagger Bx = \|Bx\|^2 > 0$ for $x \neq 0$. So we may substitute $M = AB$ in Eq. (D7) to obtain

$$\begin{aligned} \sigma_{\min}^2(AB) &= \min_{x \neq 0} \frac{x^\dagger B^\dagger A^\dagger ABx}{x^\dagger B^\dagger Bx} \frac{x^\dagger B^\dagger Bx}{x^\dagger x} \\ &\geqslant \min_{x \neq 0} \frac{x^\dagger B^\dagger A^\dagger ABx}{x^\dagger B^\dagger Bx} \min_{x \neq 0} \frac{x^\dagger B^\dagger Bx}{x^\dagger x} \\ &= \min_{x \neq 0} \frac{x^\dagger B^\dagger A^\dagger ABx}{x^\dagger B^\dagger Bx} \sigma_{\min}^2(B), \end{aligned} \tag{D8}$$

where we substituted Eq. (D7) for $M = B$.

Analogous to Eq. (D5), we bound from below the first term in the last line of Eq. (D8). Thus, we write

$$\min_{x \neq 0} \frac{x^\dagger B^\dagger A^\dagger ABx}{x^\dagger B^\dagger Bx} \geqslant \min_{y \neq 0} \frac{yA^\dagger Ay}{y^\dagger y} = \sigma_{\min}^2(A). \tag{D9}$$

The inequality in Eq. (D9) becomes an equality if and only if a right singular vector of A with its smallest singular value is in the range of B. Again, this is the case if B is square and of full rank. Substituting Eq. (D9) into Eq. (D8), we obtain the desired bound, Eq. (D2), for $\sigma_{\min}(AB)$.

If $Bx = 0$ for some $x \neq 0$, then $\sigma_{\min}(B) = 0$. Then Eq. (D2) is trivially satisfied all singular values is non-negative by definition, so $\sigma_{\min}(AB) \geqslant 0$.

Lastly, one may prove that if the left singular vector of B corresponding to $\sigma_{\min}(B)$ equals the right singular vector of A corresponding to $\sigma_{\min}(A)$, then Eq. (D2) becomes an equality. To do so, one need only to follow reasoning analogous to Eq. (D6).

---

[1] A. C. Turner-Foster, M. A. Foster, R. Salem, A. L. Gaeta, and M. Lipson, Frequency conversion over two-thirds of an octave in silicon nanowaveguides, Opt. Express **18**, 1904 (2010).

[2] Q. Lin, J. Zhang, P. M. Fauchet, and G. P. Agrawal, Ultra-broadband parametric generation and wavelength conversion in silicon waveguides, Opt. Express **14**, 4786 (2006).

[3] W. Mathlouthi, H. Rong, and M. Paniccia, Characterization of efficient wavelength conversion by four-wave mixing in sub-micron silicon waveguides, Opt. Express **16**, 16735 (2008).

[4] S. Zlatanovic, J. S. Park, S. Moro, J. M. C. Boggio, I. B. Divliansky, N. Alic, S. Mookherjea, and S. Radic, Mid-infrared wavelength conversion in silicon waveguides using

ultracompact telecom-band-derived pump source, Nat. Photonics **4**, 561 (2010).

[5] B. E. A. Saleh and M. C. Teich, *Fundamentals of Photonics*, 3rd ed., Wiley Series in Pure and Applied Optics (Wiley, Hoboken, NJ, 2019).

[6] A. Yariv and P. Yeh, *Photonics: Optical Electronics in Modern Communications*, 6th ed., Oxford Series in Electrical and Computer Engineering (Oxford University Press, New York, 2007), pp. 358–380.

[7] R. W. Boyd, *Nonlinear Optics*, 3rd ed. (Academic Press, Amsterdam, 2008), pp. 74–108.

[8] M. F. Yanik and S. Fan, Dynamic photonic structures: Stopping, storage, and time reversal of light, Stud. Appl. Math. **115**, 233 (2005).

[9] M. Notomi and S. Mitsugi, Wavelength conversion via dynamic refractive index tuning of a cavity, Phys. Rev. A **73**, 051803(R) (2006).

[10] W. Pauli, *Statistical Mechanics*, Pauli Lectures on Physics (Dover Publications, Mineola, NY, 1973), pp. 85–87.

[11] H. Goldstein, C. Poole, and J. Safko, *Classical Mechanics*, 3rd ed. (Addison Wesley, San Francisco, 2002), pp. 549–553.

[12] S. F. Preble, Q. Xu, and M. Lipson, Changing the colour of light in a silicon resonator, Nat. Photonics **1**, 293 (2007).

[13] S. Preble, L. Cao, A. Elshaari, A. Aboketaf, and D. Adams, Single photon adiabatic wavelength conversion, Appl. Phys. Lett. **101**, 171110 (2012).

[14] T. Tanabe, M. Notomi, H. Taniyama, and E. Kuramochi, Dynamic release of trapped light from an ultrahigh-*Q* nanocavity via adiabatic frequency tuning, Phys. Rev. Lett. **102**, 043907 (2009).

[15] R. Konoike, H. Nakagawa, M. Nakadai, T. Asano, Y. Tanaka, and S. Noda, On-demand transfer of trapped photons on a chip, Sci. Adv. **2**, e1501690 (2016).

[16] T. Tanabe, E. Kuramochi, H. Taniyama, and M. Notomi, Electro-optic adiabatic wavelength shifting and *Q* switching demonstrated using a pin integrated photonic crystal nanocavity, Opt. Lett. **35**, 3895 (2010).

[17] N. Karl, P. P. Vabishchevich, M. R. Shcherbakov, S. Liu, M. B. Sinclair, G. Shvets, and I. Brener, Frequency conversion in a time-variant dielectric metasurface, Nano Lett. **20**, 7052 (2020).

[18] W. Yoshiki, Y. Honda, M. Kobayashi, T. Tetsumoto, and T. Tanabe, Kerr-induced controllable adiabatic frequency conversion in an ultrahigh *Q* silica toroid microcavity, Opt. Lett. **41**, 5482 (2016).

[19] Y. Minet, L. Reis, J. Szabados, C. S. Werner, H. Zappe, K. Buse, and I. Breunig, Pockels-effect-based adiabatic frequency conversion in ultrahigh-*Q* microresonators, Opt. Express **28**, 2939 (2020).

[20] X. He, L. Cortes-Herrera, K. Opong-Mensah, Y. Zhang, M. Song, G. P. Agrawal, and J. Cardenas, Electrically induced adiabatic frequency conversion in an integrated lithium niobate ring resonator, Opt. Lett. **47**, 5849 (2022).

[21] Y. Xiao, G. P. Agrawal, and D. N. Maywar, Spectral and temporal changes of optical pulses propagating through time-varying linear media, Opt. Lett. **36**, 505 (2011).

[22] Y. Xiao, D. N. Maywar, and G. P. Agrawal, Optical pulse propagation in dynamic Fabry–Perot resonators, J. Opt. Soc. Am. B **28**, 1685 (2011).

[23] B. A. Daniel, D. N. Maywar, and G. P. Agrawal, Dynamic mode theory of optical resonators undergoing refractive index changes, J. Opt. Soc. Am. B **28**, 2207 (2011).

[24] M. Minkov, Y. Shi, and S. Fan, Exact solution to the steady-state dynamics of a periodically modulated resonator, APL Photonics **2**, 076101 (2017).

[25] M. Minkov and S. Fan, Localization and time-reversal of light through dynamic modulation, Phys. Rev. B **97**, 060301(R) (2018).

[26] M. R. Shcherbakov, P. Shafirin, and G. Shvets, Overcoming the efficiency-bandwidth tradeoff for optical harmonics generation using nonlinear time-variant resonators, Phys. Rev. A **100**, 063847 (2019).

[27] B. A. Daniel, D. N. Maywar, and G. P. Agrawal, Efficient adiabatic wavelength conversion in Gires–Tournois resonators, Opt. Lett. **36**, 4155 (2011).

[28] L. Cortes-Herrera, X. He, J. Cardenas, and G. P. Agrawal, Optimization of adiabatic frequency conversion in an all-pass resonator, Phys. Rev. A **106**, 023517 (2022).

[29] H. A. Haus, *Waves and Fields in Optoelectronics*, Prentice-Hall Series in Solid State Physical Electronics (Prentice-Hall, Englewood Cliffs, NJ, 1984), pp. 200–207.

[30] B. E. Little, S. T. Chu, H. A. Haus, J. Foresi, and J.-P. Laine, Microring resonator channel dropping filters, J. Lightwave Technol. **15**, 998 (1997).

[31] C. Manolatou, M. Khan, S. Fan, P. R. Villeneuve, H. Haus, and J. Joannopoulos, Coupling of modes analysis of resonant channel add-drop filters, IEEE J. Quantum Electron. **35**, 1322 (1999).

[32] J. D. Joannopoulos, S. G. Johnson, J. N. Winn, and R. D. Meade, *Photonic Crystals: Molding the Flow of Light*, 2nd ed. (Princeton University Press, Princeton, 2008).

[33] V. Van, *Optical Microring Resonators*, Series in Optics and Optoelectronics (CRC Press, Boca Raton, FL, 2016).

[34] A. Papoulis, Maximum response with input energy constraints and the matched filter principle, IEEE Trans. Circuit Theory **17**, 175 (1970).

[35] A. Papoulis, *Signal Analysis* (McGraw-Hill, New York, 1977).

[36] G. P. Agrawal, *Fiber-Optic Communication Systems*, 5th ed., Wiley Series in Microwave and Optical Engineering (Wiley, Hoboken, NJ, 2022).

[37] Y. Hu, M. Yu, D. Zhu, N. Sinclair, A. Shams-Ansari, L. Shao, J. Holzgrafe, E. Puma, M. Zhang, and M. Lončar, On-chip electro-optic frequency shifters and beam splitters, Nature (London) **599**, 587 (2021).

[38] L. Allen and J. H. Eberly, *Optical Resonance and Two-Level Atoms*, Interscience Monographs and Texts in Physics and Astronomy (Wiley, New York, 1975).

[39] P. Dong, S. F. Preble, J. T. Robinson, S. Manipatruni, and M. Lipson, Inducing photonic transitions between discrete modes in a silicon optical microcavity, Phys. Rev. Lett. **100**, 033904 (2008).

[40] See Supplemental Material at http://link.aps.org/supplemental/10.1103/PhysRevA.108.063514 for quantum-optical discussion of the constants of the motion in adiabatic frequency conversion in lossless coupled microrings.

[41] C. W. Gardiner and M. J. Collett, Input and output in damped quantum systems: Quantum stochastic differential equations and the master equation, Phys. Rev. A **31**, 3761 (1985).

[42] D. F. Walls and G. J. Milburn, *Quantum Optics*, 2nd ed. (Springer, Berlin, 2008).

[43] S. Fan, Ş. E. Kocabaş, and J.-T. Shen, Input-output formalism for few-photon transport in one-dimensional nanophotonic waveguides coupled to a qubit, Phys. Rev. A **82**, 063821 (2010).

[44] D. Roy, C. M. Wilson, and O. Firstenberg, Colloquium: Strongly interacting photons in one-dimensional continuum, Rev. Mod. Phys. **89**, 021001 (2017).

[45] S. Hassani, *Mathematical Physics: A Modern Introduction to Its Foundations*, 2nd ed. (Springer International Publishing, Cham, Switzerland, 2013).

[46] G. B. Arfken and H. J. Weber, *Mathematical Methods for Physicists*, 6th ed. (Elsevier Academic Press, San Diego, 2005).

[47] A. Messiah, *Quantum Mechanics* (North-Holland, Amsterdam, 1961).

[48] C. Cohen-Tannoudji, B. Diu, F. Laloë, S. Hemley, N. Ostrowsky, and D. Ostrowsky, *Quantum Mechanics*, Vol. 2 (Wiley, New York, NY, 1977).

[49] R. A. Horn and C. R. Johnson, *Matrix Analysis* (Cambridge University Press, Cambridge, 1985).

[50] G. W. Stewart and J.-g. Sun, *Matrix Perturbation Theory*, Computer Science and Scientific Computing (Academic Press, Boston, 1990).

[51] L. N. Trefethen and D. Bau, *Numerical Linear Algebra* (Society for Industrial and Applied Mathematics, Philadelphia, 1997).

[52] S. T. Thornton and J. B. Marion, *Classical Dynamics of Particles & Systems*, 5th ed. (Thomson Learning, San Diego, 2004).

[53] V. Barger and M. Olsson, *Classical Mechanics: A Modern Perspective*, 2nd ed. (McGraw-Hill, New York, NY, 1995).

[54] T. Kato, *Perturbation Theory for Linear Operators*, 2nd ed., Classics in Mathematics Vol. 132 (Springer, Berlin, 1995).

[55] M.-A. Miri and A. Alu, Exceptional points in optics and photonics, Science **363**, eaar7709 (2019).

[56] J. Wiersig, Review of exceptional point-based sensors, Photonics Res. **8**, 1457 (2020).

[57] A. Li, H. Wei, M. Cotrufo, W. Chen, S. Mann, X. Ni, B. Xu, J. Chen, J. Wang, S. Fan *et al.*, Exceptional points and non-Hermitian photonics at the nanoscale, Nat. Nanotechnol. **18**, 706 (2023).

[58] B. C. Hall, *Lie Groups, Lie Algebras, and Representations An Elementary Introduction*, Graduate Texts in Mathematics Vol. 222 (Springer New York, New York, 2003).

[59] R. P. Feynman, F. L. Vernon Jr, and R. W. Hellwarth, Geometrical representation of the Schrödinger equation for solving maser problems, J. Appl. Phys. **28**, 49 (1957).

[60] N. Frigo, A generalized geometrical representation of coupled mode theory, IEEE J. Quantum Electron. **22**, 2131 (1986).

[61] Q. Lin and G. P. Agrawal, Vector theory of four-wave mixing: Polarization effects in fiber-optic parametric amplifiers, J. Opt. Soc. Am. B **21**, 1216 (2004).

[62] J. N. Damask, *Polarization Optics in Telecommunications*, Springer Series in Optical Sciences Vol. 101 (Springer New York, New York, 2005).

[63] F. J. Harris, On the use of windows for harmonic analysis with the discrete Fourier transform, Proc. IEEE **66**, 51 (1978).

[64] E. O. Brigham, *The Fast Fourier Transform and Its Applications*, Prentice-Hall Signal Processing series (Prentice Hall, Englewood Cliffs, NJ, 1988), pp. 181–182.